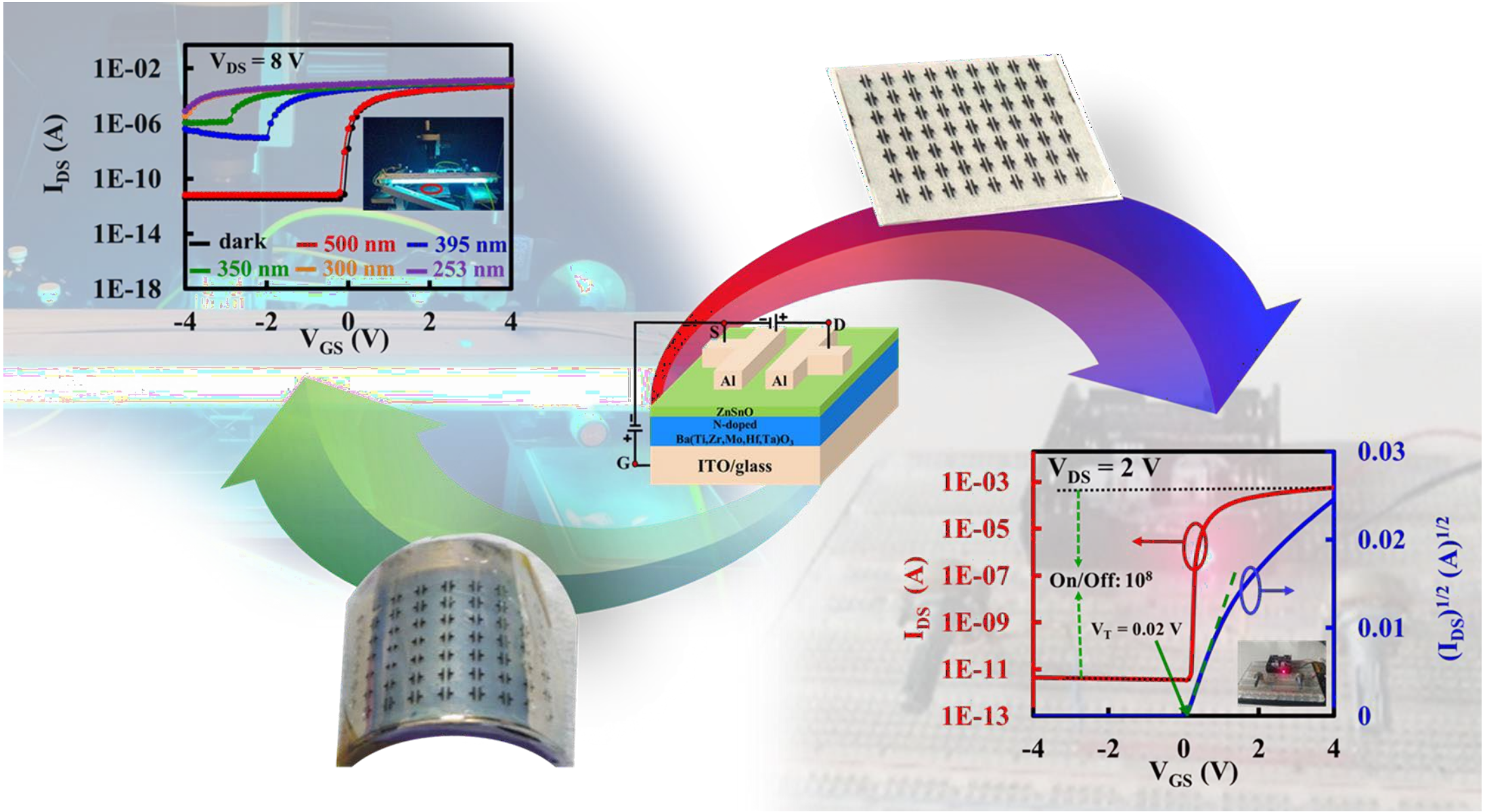

V_{DS} = 8 V
1E-02
1E-06
1E-10
1E-14
1E-18
I_{DS} (A)
dark
500 nm
395 nm
350 nm
300 nm
253 nm
-4
-2
0
2
4
V_{GS} (V)
S
D
G
Al
Al
ZnSnO
N-doped
Ba(Ti,Zr,Mo,Hf,Ta)O_3
ITO/glass
V_{DS} = 2 V
1E-03
1E-05
1E-07
1E-09
1E-11
1E-13
On/Off: 10^8
V_T = 0.02 V
0.03
0.02
0.01
0
$(I_{DS})^{1/2}$ $(A)^{1/2}$

Highlights:

- Fabrication of flexible TFTs based on N-doped $Ba(Ti,Zr,Mo,Hf,Ta)O_3$ dielectric and ZnSnO channel.
- Low equivalent oxide thicknesses (≈ 2 nm) and high-entropy (ΔS_{conf} ≈ 1.59 R) of N-doped $Ba(Ti,Zr,Mo,Hf,Ta)O_3$.
- k ≈ 262–322 and tan δ ≈ 0.01–0.30 for N-doped $Ba(Ti,Zr,Mo,Hf,Ta)O_3$.
- TFT performance: current on/off ratio of 10^8, V_T of 0.02 V, μ_{sat} of 94 $cm^2\ V^{-1}\ s^{-1}$, and S.S. of 0.062 V dec^{-1}.
- Long-term stability for up to five months.
- Small or negligible changes in V_T and drain-source current under various gate-bias stress and temperature conditions.
- S (≈ 2×10^6) and R (≈ 1171.9 A W^{-1}) of the TFT-based ultraviolet detector.
- Reliable performance in electrical or sensing characteristics under various deformations.
- Energy band diagram to elucidate the remarkable performance.

Manuscript File Click here to view linked References

Electrical and UV-Sensing Performance of N-Doped-Ba(Ti,Zr,Mo,Hf,Ta)O_3-Dielectric and ZnSnO-Channel-Based Flexible Thin-Film Transistors

Van Dung Nguyen[1], Takahiro Nagata[2], Huu Duc Luong[3], and K.-S. Chang[1,]*

[1] Department of Materials Science & Engineering, National Cheng Kung University.

No.1, University Road, Tainan City 70101, Taiwan.

[2] Research Center for Electronic and Optical Materials, National Institute for Materials Science.

1-1 Namiki, Tsukuba, Ibaraki 305-0044, JAPAN.

[3]Laboratory for Chemistry and Life Science (CLS), Institute of Innovative Research (IIR), Tokyo Institute of Technology.

R1-25, 4259 Nagatsuta-cho, Midori-ku, Yokohama, 226-8501, JAPAN.

[*]e-mail: kschang@mail.ncku.edu.tw; Tel.: +886-6-2757575 ext. 62922.

Flexible thin-film transistors (TFTs) based on N-doped Ba(Ti,Zr,Mo,Hf,Ta)O_3 dielectric and ZnSnO channel show high electrical and UV-sensing performance. The optimal N-doped Ba(Ti,Zr,Mo,Hf,Ta)O_3 compositions with low equivalent oxide thicknesses (≈ 2 nm) and high-entropy (configurational entropy ≈ 1.59 R) are efficiently determined from a wide composition space (library). The film library is patterned to 450 metal-insulator-metal stacks, revealing dielectric constants ≈ 262–322 and loss (tan δ) ≈ 0.01–0.30 for the N-doped Ba(Ti,Zr,Mo,Hf,Ta)O_3 at 1 kHz. The library is further integrated to 63 TFTs, and the promising ones exhibit the remarkable parameters: current on/off ratio of 10^8, threshold voltage (V_T) of 0.02 V, saturation field-effect mobility of 94 $cm^2\ V^{-1}\ s^{-1}$, and subthreshold swing of 0.062 V dec^{-1}. The devices also exhibit desirable long-term stability for up to five months and perform reliably with small or negligible changes in V_T and drain-source current under various gate-bias stress and temperature conditions. Furthermore, the TFT-based ultraviolet (253 nm) detector demonstrates impressive sensitivity (≈ 2×10^6) and responsibility (≈ 1171.9 A W^{-1}). There is no substantial degradation in electrical or sensing characteristics under various levels of deformation. Charge transport in constructed energy band diagrams is used to elucidate the observed remarkable performance.

Keywords: thin-film transistors, N-doped-Ba(Ti,Zr,Mo,Hf,Ta)O_3 dielectric, ZnSnO channel, flexibility, UV detector.

1. Introduction

The performance of thin-film transistors (TFTs) for next-generation electronic devices is determined by the quality of their channel and dielectric layers. For the channel material, various oxides with low cost, high transparency, and amenability to low-temperature processing (ZnO,[1–4] InGaZnO,[5–10] InZnSnO,[11] and InZnO[12]) have gained considerable attention in addition to the traditional amorphous or polycrystalline Si [13–15]. For example, Zou *et al*. fabricated HfO_xN_y dielectrics and amorphous InGaZnO-channel-based TFTs exhibiting a current on/off ratio (I_{on}/I_{off}) of 7×10^7, a saturation mobility (μ_{sat}) of 12.1 $cm^2 \cdot V^{-1} \cdot s^{-1}$, and a threshold voltage (V_T) of 0.33 V [5]. Song *et al*. reported HfLaON dielectrics and amorphous InGaZnO-channel-based TFTs with the performance parameters of $I_{on}/I_{off} \approx 1.5 \times 10^6$, μ_{sat} of 31.3 $cm^2 \cdot V^{-1} \cdot s^{-1}$, V_T of 3.4 V, and subthreshold swing (SS) of 0.22 $V \cdot dec^{-1}$[6]. For HfAlO dielectrics and InGaZnO-channel-based TFTs, Ma *et al*. reported the device parameters of $I_{on}/I_{off} \approx 1.7 \times 10^7$, μ_{sat} of 5.52 $cm^2 \cdot V^{-1} \cdot s^{-1}$, V_T of 0.83 V, and SS of 0.176 $V \cdot dec^{-1}$ [9]. Chen *et al*. fabricated $InNbTiO_2$ dielectrics and InZnO-channel-based TFTs that exhibited μ_{sat} of 1.88 $V \cdot dec^{-1}$ and SS of 0.068 $V \cdot dec^{-1}$ [12]. Despite the excellent performance of these devices, the toxicity and rarity of In and Ga elements severely limit their wide application in commercial electronics. ZnSnO is a promising alternative channel material due to its nontoxicity, elemental abundance, wide band gap (E_g), and high μ_{sat} [16–23]. For example, Wang *et al*. fabricated SiO_2 dielectrics and ZnSnO-channel-based TFTs for an ultraviolet (UV) photodetector that exhibited sensitivity (S) of 10^5 and responsivity (R) of 808 $A \cdot W^{-1}$ under a power of 124 $\mu W \cdot cm^{-2}$ [16]. Oluwabi *et al*. fabricated ZrO_x dielectrics and amorphous ZnSnO-channel-based TFTs with $I_{on}/I_{off} \approx 10^6$, μ_{sat} of 4.6 $cm^2 \cdot V \cdot s^{-1}$, SS of 0.25 $V \cdot dec^{-1}$, and V_T of 3 V [17]. Ahn *et al*. reported the performance of SiO_2 dielectrics and ZnSnO-channel-based TFTs exhibiting μ_{sat} of 13.2 cm^2 $V \cdot s^{-1}$, SS of 0.15 $V \cdot dec^{-1}$, V_T of 0.34 V, and negative bias instability of −0.2 V [18]. Allemang *et al*. revealed the characteristics of SiO_2 dielectrics and ZnSnO-channel-based TFTs, with μ_{sat} of 22 $cm^2 \cdot V \cdot s^{-1}$, SS of 0.28 $V \cdot dec^{-1}$, and turn-on voltage of –0.78 V [20]. For Yb_2O_3 dielectrics and ZnSnO-channel-based TFTs, Yang *et al*. also obtained the parameters of I_{on}/I_{off} $\approx 2.15 \times 10^7$, μ_{sat} of 9.1 $cm^2 \cdot V^{-1} \cdot s^{-1}$, V_T of 1.7 V, SS of 0.12 $V \cdot dec^{-1}$, and threshold voltage shifts (ΔV_T) of 0.06 and –0.2 V under positive and negative gate bias stress (PGBS and NGBS, respectively) [21]. However, the related research of ZnSnO in flexible electronics is still lacking due to the demanding manufacturing conditions [*e.g.*, a high deposition temperature (>350 °C)]

required to achieve desirable performance. Its high content of oxygen vacancies (V_O) also causes deterioration in the performance and reliability of the resulting devices. Furthermore, the synthesis mechanism is yet to be elucidated [17, 22, 23].

SiO_2 with a dielectric constant of $k \approx 3.9$ has traditionally been used as the dielectric layer of TFTs [16, 18, 19, 22, 23]. However, the high operating voltage (>30 V) of these TFTs significantly limits their wide application in low-power, smart, and portable devices. The aggressive scaling of SiO_2 also leads to a serious problem of substantial leakage current density (J_L) due to direct tunneling, further causing huge power consumption and poor reliability of devices [24, 25]. Various high-*k* materials including $BaSrTiO_3$ [1], HfO_2 [2, 5, 8-10], Al_2O_3 [4, 20], HfAlO [7, 9], ZrO_2 [11, 18], $InNbTiO_2$ [12], and Yb_2O_3 [21] have been developed as replacements for SiO_2. However, device performance and stability still suffer from poor surface morphology, low crystalline temperature, and high trap charge densities. Recently, high-entropy oxides (HEOs) have attracted attention in electrochemistry [26, 27], electrocatalysis [28, 29], and magnetism [30] due to their tunablility and multifunctional characteristics. Furthermore, HEOs with high *k* and low dielectric loss (tan δ) values have also been explored [31-34]. For example, Huang *et al*. reported that (Al,Ti,V,Zr,Hf)O_x films have low J_L and high *k* values (≈32) [31]. Lou *et al*. reported the dielectric properties of $Sr_{0.9}La_{0.1}(Zr_{0.25}Sn_{0.25}Ti_{0.25}Hf_{0.25})O_3$ ceramics with a *k* value of 46–47 and low tan $\delta < 0.01$ [32]. Nguyen *et al*. detailed the high *k* (≈374) and low J_L ($\approx 10^{-10}$ A·cm^{-2}) values of Ba(Ti,Zr,Ta,Hf,Mo)O_3 films [33]. Yang *et al*. revealed the low tan δ (≈0.024) and high *k* (≈110) values of $(Bi_{0.2}Na_{0.2}K_{0.2}La_{0.2}Sr_{0.2})TiO_3$ thin films [34]. These features make HEOs ideal dielectric layers for TFTs [35, 36]. For example, Salian *et al*. prepared (Co,M,nNi,Fe,Cr)O-film and MoS_2-channel-based TFTs with μ of 8.8 cm^2· V^{-1}·s^{-1}, $I_{on}/I_{off} \approx 10^5$, V_T of −1.5 V, and SS of 0.38 V·dec^{-1} [35] Liang *et al*. reported the high *k* (≈13) and low J_L ($\approx 2.9 \times 10^{-7}$ A·cm^{-2} at 2 MV·cm^{-1}) values of (HfMgTiYZr)O_x ceramics, and the resulting InZnO-channel-based TFTs featured μ_{sat} of 14.2 cm^2· V^{-1}·s^{-1}, $I_{on}/I_{off} \approx 6.3 \times 10^8$, V_T of 1.3 V, and SS of 0.34 V [36].

The use of sufficiently thick high-*k* dielectrics with compatible high-μ channel layers enables satisfactory capacitance while reducing J_L and V_T, indicating a promising approach to resolve the scaling and power consumption problems of TFTs [1-12, 17, 21, 35, 36]. However, a literature search revealed no prior investigation into the coupling of high-entropy oxynitride films and ZnSnO channel layers for next-generation flexible TFTs. Furthermore, no studies have demonstrated their superiority as UV-sensing devices.

In this study, the optimal high-entropy N-doped Ba(Ti,Zr,Mo,Hf,Ta)O_3 films on indium tin oxide (ITO)-coated glass substrates were rapidly determined from a film library that was prepared by high-throughput co-sputtering and encompassed a wide composition space. In addition to experimental characterization and theoretical calculations, the films were patterned into metal-insulator-metal (MIM) configurations and further integrated with ZnSnO channels to form TFTs, in order to study their dielectric and electrical performances and long-term reliability. Various positive and negative bias stresses with and without illumination were also applied at various temperatures to examine the stability and charge trapping effects of the resulting TFTs. Furthermore, the UV photodetection capability of the TFTs with and without various levels of deformation revealed impressive performance and flexibility of the device. Finally, energy band diagrams of the devices were constructed to elucidate their remarkable characteristics.

2. Experimental Section

Fabrication of N-doped Ba(Ti,Zr,Mo,Hf,Ta)O_3 film library

The N-doped Ba(Ti,Zr,Mo,Hf,Ta)O_3 film library was deposited on ITO/glass substrates through high-throughput radio-frequency (RF) co-sputtering using two targets: a $BaTiO_3$ target (99.9%, Ultimate Materials Technology Co. Ltd., Taiwan) and a (Zr,Mo,Hf,Ta) sliced target (99.9%, Ultimate Materials Technology Co. Ltd., Taiwan). The sputtering chamber was vacuumed to approximately 3.0×10^{-6} Torr. Then, deposition was performed for 2 h using the RF powers of 70 and 150 W for the $BaTiO_3$ and (Zr,Mo,Hf,Ta) targets, respectively, at a working pressure of 15 mTorr and room temperature under a gas flow of $Ar:O_2:N_2$ = 30:10:3 (sccm).

Fabrication of N-doped Ba(Ti,Zr,Mo,Hf,Ta)O_3-based metal-insulator-metal (MIM) stack library

The N-doped Ba(Ti,Zr,Mo,Hf,Ta)O_3-based MIM stack library was fabricated by depositing Al metal onto the prepared film library using a stainless-steel physical mask. Metal deposition was conducted via direct current (DC)-100-W sputtering for 30 min at 15 mTorr (18 sccm Ar flow) and room temperature. A total of 450 MIM configurations were formed on the film library, and they were subjected to FGA (90% N_2 + 10% H_2) at 350 °C for 40 min.

Fabrication of N-doped Ba(Ti,Zr,Mo,Hf,Ta)O_3-based TFT library

The N-doped Ba(Ti,Zr,Mo,Hf,Ta)O_3-based TFT library was fabricated as follows. An ITO-coated glass substrate with deposited N-doped Ba(Ti,Zr,Mo,Hf,Ta)O_3 film library was used as the bottom gate. ZnSnO channel layers were then deposited on the N-doped

Ba(Ti,Zr,Mo,Hf,Ta)O_3 film library by RF-100-W co-sputtering of Sn and Zn targets (99.9%, Ultimate Materials Technology Co., Ltd., Taiwan) for 20 min at 5 mTorr [Ar:O_2 = 18:2 (sccm)] and room temperature. The resultant configuration was annealed at 350 °C in air for 60 min. Al metal was subsequently deposited and patterned as source and drain electrodes using DC-100-W sputtering through another stainless-steel physical mask, in which ZnSnO channels were formed with a length of 170 μm and a width of 1700 μm. A total of 63 TFTs were formed on the film library, followed by FGA at 350 °C for 40 min.

Characterization

Hybrid-DFT was used to calculate the energy band structures of N-doped Ba(Ti,Zr,Mo,Hf,Ta)O_3 and ZnSnO. High-throughput XRF (Shimadzu, μEDX1400, Japan) and XRD (D8 DISCOVER, BL15XU NIMS beamline, Japan) were used to analyze the elemental composition and phase/crystallinity of the N-doped Ba(Ti,Zr,Mo,Hf,Ta)O_3 film library, respectively. XPS (PHI VersaProbe 4, USA) was used to determine the binding and valence states of the constituent elements in the samples. The E_g values of the N-doped Ba(Ti,Zr,Mo,Hf,Ta)O_3 and ZnSnO films were determined using ultraviolet-visible (UV-Vis) spectroscopy (LAMBDATM 950, PerkinElmer, Inc., USA). Their work functions (Φ_s) and valence band maxima (E_{Vmax}) were determined through ultraviolet photoelectron spectroscopy (UPS). The oxide capacitance (C_{ox}) and J_L of 100 MIM stacks on the library were measured using an inductance-capacitance-resistance meter (HP4284A, Palo Alto, USA) and a semiconductor parameter analyzer (HP4145B, Palo Alto, USA), respectively. HRTEM was used to evaluate the thickness of each layer in the TFT. Furthermore, a semiconductor parameter analyzer was used to measure the output [drain-source current (I_{DS}) against drain-source voltage (V_{DS}) at various gate-source voltages (V_{GS})] and transfer (I_{DS} against V_{GS} at V_{DS} = 2 V) characteristics of the TFTs along the direction of composition variation (upper left to lower right) in the library. The transfer characteristics of the TFTs were also investigated under various PGBS and NGBS with and without 395-nm UV illumination and also under various temperatures (room temperature, 50, 100, 150, and 180 °C). TFT-based photodetectors were examined under illumination at various wavelengths (250, 300, 350, 395, and 500 nm) at a power density of 7.5 $mW \cdot m^{-2}$. Flexible photodetectors were fabricated on PI substrates to measure their transfer characteristics under various levels of deformation and examine their application in flexible electronics.

3. Results and Discussion

Materials characterization

The hybrid-density functional theory (hybrid-DFT) calculation results of the N-doped Ba(Ti,Zr,Mo,Hf,Ta)O_3 film ($E_g \approx 3.95$ eV) and ZnSnO channel layer ($E_g \approx 3.65$ eV) by setting their Fermi levels (E_F) to 0 are displayed in **Figure 1a** and **1b**, respectively. The resulting conduction band offset ($E_{C,\ offset} \approx 1.39$ eV) is sufficient (>1 eV) to block electrons in the conduction band (E_C) of ZnSnO from transport to that of N-doped Ba(Ti,Zr,Mo,Hf,Ta)O_3 (**Figure 1c**), fulfilling one of the crucial requirements for N-doped Ba(Ti,Zr,Mo,Hf,Ta)O_3 as gate dielectrics in TFTs.

A total of 100 locations across the N-doped Ba(Ti,Zr,Mo,Hf,Ta)O_3 film library, approximately 2 mm apart from each other in the x- and y-directions (top-left inset of **Figure 2a**), were characterized using high-throughput scanning X-ray diffraction (XRD). Their diffraction patterns are jointly plotted in a three-dimensional (3D) diagram (x: 2θ, y: location, and z: intensity; Figure 2a), and the top-view image is displayed in the top-right inset of Figure 2a. No diffraction peaks, indicating amorphous or nanocrystalline states, were observed in the measured 2θ range over the entire sample, due to the highly disordered (high-entropy) structures of the library and enhanced thermal stability after incorporating nitrogen [37]. As is shown later, the amorphousness caused a low leakage current for N-doped Ba(Ti,Zr,Mo,Hf,Ta)O_3 in the MIM (**Figure 5b**) and TFT (**Figure 7c**) devices. The scanning X-ray fluorescence (XRF) results of more than 400 locations on the N-doped Ba(Ti,Zr,Mo,Hf,Ta)O_3 film library are displayed in **Figure S1**. The elemental variations (at.%) across the library are elucidated in a ternary diagram with three axes for (Ba + Ti), (Ta + Hf), and (Zr + Mo) (**Figure 2b**). Based on the obtained elemental concentrations, we calculated the configurational entropies (ΔS_{conf}) at the 100 locations (shown in the top-left inset of Figure 2a) and plotted them in a 3D ternary diagram (**Figure 2c**). All the ΔS_{conf} values are greater than 1.4 R, and the regions with $\Delta S_{conf} > 1.5$ R (colored blue, orange, and green) indicate the formation of multi-principal-element (or high-entropy) oxynitride films [33].

For one of the favorable compositions in the library with $\Delta S_{conf} \approx 1.59$ R (red mark in Figure 2c with Ba:Ti:Ta:Hf:Zr:Mo ≈ 0.41:0.10:0.07:0.08:0.19:0.15 at.%), the corresponding X-ray photoelectron spectroscopy (XPS) results are shown in **Figure 3**. A deconvolution algorithm was applied to all spectra to determine the constituent elements and their valence states. In the Ba 3d spectrum (**Figure 3a**), one deconvoluted subset with two green subpeaks at approximately 779.8 and 794.9 eV is associated with lattice Ba^{2+} (L) in the perovskite structure, and another subset with two blue subpeaks at approximately 781.68 and 796.78 eV is attributable to surface Ba^{2+} (S) in the perovskite structure [38-40]. The ratio of Ba^{2+} (L):Ba^{2+}

(S) ≈ 80:20 (at.%) indicates the predominance of Ba^{2+} (L). The Ti 2p spectrum (**Figure 3b**) reveals one deconvoluted subset with two blue subpeaks at approximately 457.8 and 463.4 eV, ascribed to Ti^{3+} $2p_{3/2}$ and Ti^{3+} $2p_{1/2}$, respectively, originating from the Ti–O bonding in Ti_2O_3 and the Ti–N–O bonding in TiON. Another subset with two green subpeaks at approximately 458.7 and 464.3 eV is associated with Ti^{4+} $2p_{3/2}$ and Ti^{4+} $2p_{1/2}$, respectively, stemming from the Ti–O bonding in TiO_2 [41, 42]. The ratio of Ti^{3+}:Ti^{4+} ≈ 33:67 (at.%) implies the predominance of Ti^{4+}. In the Ta 4f spectrum (**Figure 3c**), two deconvoluted green peaks at 26.6 and 28.8 eV are respectively associated with Ta^{5+} $4f_{7/2}$ and Ta^{5+} $4f_{5/2}$ in Ta_2O_5 [43, 44]; while two blue peaks at approximately 25.6 and 27.3 eV are associated with Ta^{4+} $4f_{7/2}$ and Ta^{4+} $4f_{5/2}$, respectively, contributed by the Ta–O bonding in TaO_2 and the Ta–O–N bonding in TaON [43, 44]. The ratio of Ta^{5+}:Ta^{4+} ≈ 76:24 (at.%) suggests the predominance of Ta^{5+}(high-valence state caused by N doping). The Hf 4f spectrum (**Figure 3d**) displays two deconvoluted green subpeaks at approximately 16.2 and 18.0 eV associated with Hf^{4+} $4f_{7/2}$ and Hf^{4+} $4f_{5/2}$, respectively, because of the Hf–O bonding in HfO_2 [45, 46]. Two blue subpeaks at approximately 15.6 and 17.28 eV are attributable to Hf^{x+} $4f_{7/2}$ and Hf^{x+} $4f_{5/2}$, respectively, due to the Hf–O bonding in suboxides [45, 46] and the Hf–O–N bonding in HfON [45]. The ratio of Hf^{4+}:Hf^{x+} ≈ 65:35 (at.%) indicates the predominance of Hf^{4+}. In the Zr 3d spectrum (**Figure 3e**), the green deconvoluted subset of peaks at approximately 181.42 and 183.7 eV is attributable to Zr^{x+} $3d_{5/2}$ and Zr^{x+} $3d_{3/2}$, respectively, because of the Zr^{x+}–O bonding in suboxides [47] and the Zr–O–N bonding in ZrO_xN_y [48]. Another purple subset comprising peaks at 183.47 and 185.84 eV is associated with Zr^{4+} $3d_{5/2}$ and Zr^{4+} $3d_{3/2}$, respectively, because of the Zr^{4+}–O bonding in ZrO_2 [47, 48]. The ratio of Zr^{4+}:Zr^{x+} ≈ 70:30 (at.%) reflects the predominance of Zr^{4+}. Moreover, the blue peak is attributed to Ba $4p_{3/2}$. The Mo 3d spectrum (**Figure 3f**) reveals two deconvoluted green peaks at approximately 232.5 and 235.6 eV that are attributable to Mo^{6+} $3d_{5/2}$ and Mo^{6+} $3d_{3/2}$, respectively, because of the Mo^{6+}–O bonding in MoO_3. Two deconvoluted blue peaks at approximately at 229.9 and 233.0 eV are associated with Mo^{4+} $3d_{5/2}$ and Mo^{4+} $3d_{3/2}$, respectively, because of the Mo^{4+}–O bonding in MoO_2 and the N–Mo–O bonding in MoON [49]. The ratio of Mo^{6+}:Mo^{4+} ≈ 80:20 (at.%) indicates the predominance of Mo^{6+} (high-valence state caused by N doping). The O 1s spectrum (**Figure 3g**) shows four subpeaks: metal (M)–O bonding at approximately 529.9 eV, M–N–O bonding at approximately 531.1 eV, V_O (≈14.3 at.%) at 531.75 eV, and H–O bonding (H_2O) at approximately 533.12 eV [42, 50]. The N 1s spectrum (**Figure 3h**) exhibits a broad peak at 395.2–402 eV, which was deconvoluted into two subpeaks at 397.6 eV (green) due to M–N–O bonding and 399.6 eV (purple) due to chemisorbed nitrogen (N_C). Moreover, the blue peak at 404.4 eV is associated with Ta $4p_{3/2}$ [43]. From the calculated

peak areas of each element, the film composition was determined to be Ba:Ti:Zr:Mo:Hf:Ta:O:N ≈ 0.2:0.04:0.07:0.06:0.03:0.03:0.57:0.01 (at.%), which is equivalent to $Ba(Ti_{0.17}Zr_{0.30}Mo_{0.26}Hf_{0.13}Ta_{0.13})(O_{2.9}N_{0.1})$. This stoichiometry is consistent with the XRF results when O and N are not considered (Figure 2b). The composition was further evaluated by transmission electron microscopy-energy dispersive X-ray spectroscopy (TEM-EDS) analysis (**Figure 4**).

Figure 4 shows the TEM-EDS analysis result of one TFT device composed of N-doped $Ba(Ti,Zr,Mo,Hf,Ta)O_3$ in the high-entropy region (red circle in Figure 2c). **Figure 4a** shows the mapping area (red square), and **Figure 4b**(i)–(xii) illustrate the distribution of each element. In general, all metallic elements are homogeneously scattered without diffusion between the layers (Figure 4b(i)–(xi)). The O signals are clearly observed in the three oxide layers of ZnSnO, N-doped $Ba(Ti,Zr,Mo,Hf,Ta)O_3$, and ITO (Figure 4b(xi)). The distribution of N is not shown due to its low concentration; however, its signals are observed in the spectrum (**Figure 4c**). Our analysis reveals the robust formation of an Al electrical terminal (Figure 4b(i)), a ZnSnO channel [Zn and Sn signals in Figure 4b(ii) and (iii, upper part), respectively], an ITO bottom gate [Sn and In signals in Figure 4b(iii, lower part) and (iv), respectively], and N-doped $Ba(Ti,Zr,Mo,Hf,Ta)O_3$ dielectrics (Figure 4b(v)–(xi)). Figure 4c displays an associated spectrum of the mapping area, which quantitatively determines the atomic ratio as Ba:Ti:Zr:Mo:Hf:Ta:O:N ≈ 0.18:0.04:0.07:0.06:0.03:0.03:0.58:0.01, which is consistent with the XPS result (Figure 3) and also in accordance with the XRF result when O and N are not considered (Figure 4).

Dielectric property of N-doped $Ba(Ti,Zr,Mo,Hf,Ta)O_3$ film library

To measure the dielectric properties of N-doped $Ba(Ti,Zr,Mo,Hf,Ta)O_3$, the film was patterned into a MIM configuration and subjected to various FGA conditions to minimize interfacial defects (D_{it}). From our capacitance–voltage (C–V) and current density–voltage (J_L–V) measurements, the configuration treated with FGA at 350 °C for 40 min exhibited the most promising dielectric properties (**Figure S4**). This impressive improvement is attributed to the following three factors. (1) The incorporation of N passivates the unsaturated dangling bonds and V_O in the sample. (2) Nitrogen hinders metal diffusion, minimizing the formation of unexpected defects and resulting in a distinct interface between N-doped $Ba(Ti,Zr,Mo,Hf,Ta)O_3$ and ITO (**Figure 6**) [6]. (3) The highly disordered N-doped $Ba(Ti,Zr,Mo,Hf,Ta)O_3$ effectively reduces the flowing paths for J_L [36]. The optimal FGA conditions were then applied to the entire library-based MIM configurations (a total of 450 devices), and 100 of them (at the same locations as shown in Figure 2a) were investigated

(**Figure 5**). **Figure 5a** and **5b** show the 3D ternary diagrams of C_{ox} measured at 1 kHz and J_L measured at 1 V against the elemental compositions, respectively. In general, C_{ox} gradually increases and J_L gradually decreases toward lower concentrations of Ba and Ti and higher concentrations of Zr and Mo (white line). The dashed black circles in the two figures denote favorable compositions that have reasonably high C_{ox} and low J_L values.

To quantify the *k* and tan δ values of N-doped Ba(Ti,Zr,Mo,Hf,Ta)O_3, high-resolution transmission electron microscopy (HRTEM) cross-sectional images were captured to determine the thickness of each layer in the TFT devices (Figure 6). Four different TFT devices along the direction of composition variation (**Figure 6a**) in the film library were examined to enhance the measurement accuracy (**Figure 6b**(i)–(iv)). From the images, all devices are composed of four layers with clear interfaces (consistent with Figure 4), namely ITO (bottom gate), amorphous N-doped Ba(Ti,Zr,Mo,Hf,Ta)O_3 (≈133.4–162.6 nm), ZnSnO (≈28.7–31.0 nm), and Al (source/drain terminal), indicating satisfactory film quality in these devices. The thickness variation of N-doped Ba(Ti,Zr,Mo,Hf,Ta)O_3 is due to the natural composition spread of the co-sputtering approach.

The measured C_{ox} in those 100 MIM devices (**Figure 5a**) is contributed by the N-doped Ba(Ti,Zr,Mo,Hf,Ta)O_3 dielectric layer. Based on its thickness, we extracted the *k* values (≈262–322 at 1 kHz) of N-doped Ba(Ti,Zr,Mo,Hf,Ta)O_3 with an area of ≈ 2.0×10^{-7} m^2/device and plotted them in a 3D ternary diagram (**Figure 7a**). The associated equivalent oxide thickness (EOT) of N-doped Ba(Ti,Zr,Mo,Hf,Ta)O_3 across the library was also determined (≈1.79–2.21 nm) and plotted in a 3D ternary diagram based on the *k* values (**Figure 7b**). The calculation details of the *k* and EOT values are discussed in our previous reports.[31, 33] Figure 7c illustrates the associated tan δ values (≈0.01–0.30) characterized at 1 kHz. In these figures, the dotted black circles in the composition range (Ba + Ti) = 51.9–59.5 at.%, (Mo + Zr) = 24.1–33.1 at.%, and (Ta + Hf) = 14.9–16.3 at.% manifest the compositions with low EOT (<1.94 nm), remarkable charge storage capability (*k* ≈ 300–322), and low tan δ (≈0.01–0.06) due to the synergistically enhanced ΔS_{conf} of the films, as discussed in Figure 2c. These characteristics are superior to those reported in the literature [31, 34-36] indicating that our films are promising for TFT applications.

Electrical performance of N-doped Ba(Ti,Zr,Mo,Hf,Ta)O_3-based TFT library

The entire library was patterned into 63 TFTs (upper right inset, **Figure 8a**) and their electrical performance was examined. Here, we discuss the representative results for one of the favorable devices (red mark in the upper right inset of Figure 8a). The voltage supplies among the source (Al), drain (Al), and bottom-gate (ITO) terminals are illustrated in the lower right

inset of Figure 8a, and the output characteristics measured at V_{GS} = 0–4 V are depicted in Figure 8a. The correlation between I_{DS} and V_{DS} indicates a typical n-channel transistor with distinct pinch-off and saturated current characteristics. I_{DS} is not observed at V_{GS} = 0 because no charge transport channel was formed in ZnSnO. A linear increase in I_{DS} at low V_{DS} for each V_{GS} (>0 V) reveals a desirable ohmic contact between the source (or drain) electrode and ZnSnO.[24] **Figure 8b** presents the transfer characteristics of the device [I_{DS} against V_{GS} at V_{DS} = 2 V (red curve)], which also suggests an n-type characteristic with a remarkable current on/off ratio of 10^8. Based on the transfer characteristics, the plot of $(I_{DS})^{1/2}$ against V_{GS} (blue curve) is used to extract the associated device parameters of $\mu_{sat} \approx 94$ cm^{-2} V^{-1} s^{-1} and $V_T \approx 0.02$ V. The derivative $\partial V_{GS}/\partial \log(I_{DS})$ was further calculated to obtain SS ≈ 0.062 V dec^{-1} and $D_{it} \approx 9.59 \times 10^{10}$ eV^{-1} cm^{-2}. The calculation for obtaining these parameters is detailed in our previous report [42]. Our devices here outperform other high-*k*-based devices reported in the literature (**Table 1**) [17, 19, 51-54]. This superiority is partially attributable to the incorporation of N[6] and the sluggish diffusion effect [55] that restrict the grain growth of N-doped Ba(Ti,Zr,Mo,Hf,Ta)O_3, preserving its amorphous structure (**Figure 2b**). The resulting TFT applied to a circuit board as a switch is displayed in the lower right inset of Figure 8b, where the photodiode lights up when the TFT is switched on. Furthermore, the long-term stability of the TFT was examined by placing it in a desiccator at 30% humidity and room temperature for one and five months. The transfer characteristics exhibit almost negligible changes compared to those of the fresh device on day 0 (**Figure 8c**). The corresponding μ_{sat} and SS values are illustrated in the inset of Figure 8c, and the tiny monthly variations indicate desirable long-term stability of our TFTs.

To examine the aging (reliability) performance of the TFT, the positive gate-bias stress instability (PGBSI) at V_{DS} = 2 V with and without UV illumination (395 nm) was investigated at room temperature (**Figure 9**). The PGBSI measurement procedure is illustrated in the lower right inset of **Figure 9a**. An I–V characteristic without any bias stress was initially measured, followed by another I–V characteristic measurement after the positive gate-bias stress (PGBS) was applied at 3 V for 100 s. To ensure full recovery of the TFT from the previous stress, a 15-min waiting time was applied before conducting another I–V measurement. Four other PGBS times (500, 1000, 2000, and 3600 s) were also studied for a full cycle measurement. Our results generally reveal almost constant trends for all transfer characteristics under these conditions (0–3600 s) without UV illumination, with just trivial changes in the current on/off ratio and SS (**Figure S5a**) and negligible changes in $I_{DS,\,max}$ (**Figure 9a**), which are further elucidated in the upper left inset (blue curve). These features indicate that no operation adjustment is required to

turn the device on and off, and there is no deterioration in the current flow [56]. These curves also exhibit remarkable stability with only small positive V_T shifts ($\Delta V_T \approx 0.08$ V) when the PGBS time increases from 0 to 3600 s, as elucidated in the upper left inset (orange curve) of Figure 9a. An energy band diagram under the PGBS conditions is shown in **Figure 9b**, which was obtained from the associated diagram before and after contact without any stress (**Figure S6**). The downward energy band bending of ZnSnO at the N-doped Ba(Ti,Zr,Mo,Hf,Ta)O_3/ZnSnO interface facilitates the trapping of electrons induced by the positive electric field by shallow-level oxygen-related defects (acceptor-like traps) in the E_g of N-doped Ba(Ti,Zr,Mo,Hf,Ta)O_3. When the PGBS time increases, more electrons are induced, trapped, and distributed in the deep levels of the gap or into bulk N-doped Ba(Ti,Zr,Mo,Hf,Ta)O_3, thus lowering the charge carrier concentration in the channel and leading to a minor increase in V_T ($\Delta V_T \approx 0.08$ V) [56-58]. When the device is additionally subjected to UV illumination (**Figure 9c**), all transfer curves at various PGBS times (0–3600 s) exhibit negligible changes in the current on/off ratio and SS (**Figure S5b**) and $I_{DS,\,max}$ (blue curve, inset of Figure 9c), and a small positive ΔV_T (≈0.058 V) is also observed (orange curve, inset of Figure 9c). However, relative to the curves without UV illumination (Figure 9a), all UV-illuminated curves exhibit higher SS values because of more induced traps and more negative shifts in V_{GS} owing to higher charge-carrier concentrations in the channel resulting from the generation of electron–hole pairs by the light absorption of ZnSnO. The associated energy band diagram is depicted in **Figure 9d**, illustrating the illumination-induced generation of extra charge carriers and electron trapping. The negative gate-bias stress instability (NGBSI) of the device with and without UV illumination was also studied, as shown in **Figure S7** and **S8**.

To further evaluate the temperature-associated aging (reliability) problems of the TFT, the positive gate-bias temperature stress instability (PGBTSI) was studied at PGBS = 3 V, V_{DS} = 2 V, and four different temperatures (50, 100, 150, and 180 °C) for various stress times (0—–3600 s) (**Figure 10**). In general, the negligible changes in $I_{DS,\,max}$ of all transfer curves under all the conditions indicate stable device performance (blue curve, insets of **Figure 10a–d**). The trend of positive ΔV_T with increasing PGBS time from 0 to 3600 s at each temperature is also consistent with the results obtained at room temperature (Figure 9a). However, the ΔV_T at elevated temperatures (≈0.12, 0.15, 0.2, and 0.26 V at 50, 100, 150, and 180 °C after 3600 s, orange curves in the insets of Figure 10a–d, respectively) is higher than that (≈0.08 V) observed at room temperature (Figure 9a). This is ascribed to the generation of more traps at higher temperatures, resulting in more captured electrons and fewer charge carriers in the channel [59].

Furthermore, when the temperature increases from 50 to 180 °C for each PGBS time, the associated V_T value shifts more negatively in V_{GS} (*i.e.*, V_T = –0.04, –0.09, –0.15, and –0.22 V at 50, 100, 150, and 180 °C for 0 s, respectively), revealing more thermally induced electrons flowing in the channel, which can be rationalized using a thermal activation process (kinetics) of electrons (**Figure 11**).

The charge trapping kinetics in the TFT was investigated by studying the conductance activation energy (E_A). The calculation results are shown in **Figure S9**. Figure 11 shows the plots of ln(I_{DS}) against 1/KT (K: Boltzmann's constant, T: room temperature–180 °C) at various V_{GS} values for the TFT devices with and without PGBS and UV illumination. The $E_A(V_{GS})$ at each V_{GS} was then obtained from the slope of each curve and plotted in the inset of each figure. A small (large) E_A at high (low) V_{GS} implies on (off) states of the device, and the slope near a subthreshold region (dashed red line) indicates the number of traps in the system (steeper slope = fewer traps). In general, none of the E_A in the off state (low V_{GS}) vary substantially (insets of **Figure 11a–d**), and the device without PGBS or illumination treatment exhibits the fewest traps (slope ≈ 0.94 $eV \cdot V^{-1}$, inset of Figure 11a). However, more traps were induced in the device under either UV illumination only (slope ≈ 0.655 $eV \cdot V^{-1}$, inset of Figure 11b) or PGBS only (slope ≈ 0.875 $eV \cdot V^{-1}$, inset of Figure 11c), as indicated by their lower slope values. When the device was subjected to both PGBS and illumination (inset of Figure 11d), their synergistic effects on the induction of traps and electron–hole pairs led to the smallest slope (≈0.625 $eV \cdot V^{-1}$) and the most negatively shifted curve in V_{GS}. Furthermore, the impact of illumination on the generation of more carriers in the channel is also revealed by the distinct negatively shifted curves in V_{GS} (insets of Figure 11b and d) relative to those without UV illumination (insets of Figure 11a and c). The effects of NGBS and UV illumination from room temperature to 180 °C were also studied, as shown in **Figure S9**.

UV-sensing capability of N-doped Ba(Ti,Zr,Mo,Hf,Ta)O_3-based TFT library

The UV-sensing capability of the TFT was studied by illuminating the device at wavelengths of 253, 300, 350, 395, and 500 nm (**Figure 12**). A photograph of the measurement setup under illumination is displayed in the inset of **Figure 12a**, and the associated transfer curves are depicted in Figure 12a. When the device is exposed to visible light (500 nm, red curve), a slightly negative ΔV_T compared with the dark curve (no illumination, black curve) is observed. In contrast, under UV light the transfer curves shift remarkably toward negative V_{GS} (negative ΔV_T) and shift up (high I_{DS}) at an off state, indicating substantially enhanced current flow at negative V_{GS}. These characteristics are attributable to the formation of considerable

amounts of photon-induced electron–hole pairs. **Figure 12b** shows the output curves of the device measured at V_{GS} = –6 V, which ensures the robust formation of a depletion region (off-current state) for the device. When the device is in the dark (black curve) and under 500-nm illumination (red curve), negligible I_{DS} at any V_{DS} reveals the off state of the device. This behavior is explained by the energy band diagram depicted in the upper right inset of Figure 12b, in which negative V_{GS} results in the upward band bending of ZnSnO at the N-doped Ba(Ti,Zr,Mo,Hf,Ta)O_3/ZnSnO interface. This pushes electrons away from the interface, causing them to be subsequently captured by surface oxygen ($O_2 + e^- \rightarrow O_2^-$) to form a widened depletion region. Thus, no carrier flow occurs in the ZnSnO channel. However, when the device was illuminated by UV light (253–395 nm), noticeable I_{DS} is observed. In this scenario, electrons in ZnSnO are generated through multiple processes including (1) the induction of electron–hole pairs, (2) the ionization of neutral V_O to V_O^{2+} by hole capture (as discussed in Figure S2 and S3), and (3) the oxidation of surface ionized oxygen molecules ($O_2^- \rightarrow e^- + O_2$) (lower right inset of Figure 12b). Furthermore, the resulting V_O^{2+} is attracted to the interface to screen the negative V_{GS} effect on the resulting electrons. Thus, excessive accumulation of these electrons reduces the depletion width, causing a net increase in I_{DS} in the channel. The UV–visible rejection ratio of the device, estimated from the photocurrents measured at 253 and 500 nm, is approximately 10^6, revealing remarkable UV recognition capability of the device. **Figure 12c** shows the photocurrent durability measured at V_{GS} = –6 V and V_{DS} = 8 V under various UV illuminations. The photocurrent systematically increases when exposed to shorter wavelengths (higher excitation energies). Repeatable and stable photocurrent responses without noticeable degradation after five cycles indicate the excellent reliability of the device. A single-cycle evolution of the photocurrent response (time-dependent I_{DS} curve) under 253-nm illumination was further studied to deduce the crucial parameters of S and R for the device (**Figure 12d**). The signal abruptly increases to a saturated value in 0.037 s under illumination and dramatically decreases to zero current in 0.025 s without illumination. The S and R values were then determined as $S = (I_{light} - I_{dark})/I_{dark} \approx 2 \times 10^6$ and $R = (I_{light} - I_{dark})/P \approx 1171.9\ A \cdot W^{-1}$, in which I_{light}, I_{dark}, and P denote the drain current under illumination, drain current in the dark, and incident UV power, respectively. The response times and obtained device parameters surpass those of other TFT-based UV photodetectors reported in the literature (**Table 2**), implying that our TFTs are very promising for use in UV detectors.

To investigate the applicability of our device in flexible electronics, TFTs were fabricated on polyimide (PI) substrates. **Figure 13a** shows the transfer curve (red) measured at room temperature, which also indicates the n-type mode, with an excellent current on/off ratio of 10^7.

The device parameters, including $\mu_{sat} \approx 73$ $cm^{-2} \cdot V^{-1} \cdot s^{-1}$, $V_T \approx -0.02$ V, SS ≈ 0.089 $V \cdot dec^{-1}$, and $D_{it} \approx 5.94 \times 10^{12}$ eV^{-1} cm^{-2}, are extracted from the blue curve [$(I_{DS})^{1/2}$ against V_{GS}]; and they are still comparable to those of the device fabricated on rigid ITO/glass substrates (**Figure 8**), suggesting the compatibility of N-doped Ba(Ti,Zr,Mo,Hf,Ta)O_3 with flexible substrates. **Figure 13b** shows the transfer curves of the device at various bending levels with the radius (R) of 5, 8, and 12 mm (a smaller R denotes a more serious deformation). A photograph of the device bent at R = 8 mm is shown in the inset of Figure 13b. Compared to the I_{on} and I_{off} of the non-deformed device, only the device bent at R = 5 mm exhibits slightly lower I_{on} and higher I_{off}, indicating its impressive resilience. The UV-sensing (253 nm) durability of the TFT bent at R = 12 nm was studied at $V_{GS} = -6$ V and $V_{DS} = 8$ V (**Figure 13c**). The I_{DS} still remains stable and repeatable after five testing cycles, and excellent S ≈ 10^6 and R ≈ 1012 $A \cdot W^{-1}$ values are obtained. The electrical performance of the device obtained at various bending levels is summarized using a radar plot (**Figure 13d**). Compared to the case without any deformation, no noticeable degradation due to deformation is observed, revealing the great flexibility of our device.

4. Conclusions

An amorphous high-entropy N-doped Ba(Ti,Zr,Mo,Hf,Ta)O_3 dielectric film library was fabricated through co-sputtering and characterized using high-throughput scanning XRD and XRF. XPS was used to evaluate the elemental composition of the N-doped Ba(Ti,Zr,Mo,Hf,Ta)O_3 and ZnSnO channel materials, and revealed the formation of V_O in these films. The resulting TFTs exhibited remarkable long-term stability and electrical characteristics with a current on/off ratio ≈10^8, V_T of 0.02 V, $\mu_{sat} \approx 94$ cm^2 V^{-1} s^{-1}, and SS of 0.062 $V \cdot dec^{-1}$, as well as desirable stability under PGBS and NGBS at different temperatures. The TFT-based photodetector exhibited quick responses to UV illumination, remarkable S (≈ 2×10^6) and R (≈ 1171.9 $A \cdot W^{-1}$) values at 253 nm, and excellent flexibility under various levels of deformation. Energy band diagrams of the devices were constructed to elucidate their excellent performance. Our results highlight the great potential of N-doped Ba(Ti,Zr,Mo,Hf,Ta)O_3 for next-generation flexible electronic devices.

Acknowledgements

This work was partially supported by the National Science and Technology Council of Taiwan under grant numbers MOST 112-2224-E-006-003 and MOST 111-2224-E-006-005.

CRediT authorship contribution statement

Van Dung Nguyen: Data curation, Formal analysis, Investigation, Methodology, Software, Visualization, Roles/Writing – original draft. **Takahiro Nagata:** Formal analysis, Investigation, Methodology. **Huu Duc Luong:** Software. **K.-S. Chang:** Conceptualization, Data curation, Funding acquisition, Methodology, Project administration, Resources, Supervision, Validation, Writing – review & editing.

References

[1]. K.T. Kang, M. H. Lim, H.G. Kim, Il.D. Kim, J.M. Hong, High field-effect mobility ZnO thin-film transistors with Mg-dope $Ba_{0.6}Sr_{0.4}TiO_3$ gate insulator on plastic substrates, Appl. Phys. Lett. 90 (2007) 043502. http://dx.doi.org/10.1063/1.2434150.

[2]. M. Esro, G. Vourlias, C. Somerton, W.I. Milne, G. Adamopoulos, High-mobility ZnO thin film transistors based on solution-processed hafnium oxide gate dielectrics, Adv. Funct. Mater.25 (2015) 134–141. https://doi.org/10.1002/adfm.201402684.

[3]. P. Gogoi, R. Saikia, U.J. Mahanta, Oxygen annealed ZnO–La_2O_3 TFTs fabricated using CBD technique, J. Phys.: Conf. Ser. 1330 (2019) 012007. https://doi.org/10.1088/1742-6596/1330/1/012007.

[4]. H. Xu, X. Ding, J. Qi, X. Yang, J. Zhang, A Study on Solution-Processed Y_2O_3 Films Modified by Atomic Layer Deposition Al_2O_3 as Dielectrics in ZnO Thin Film Transistor, Coatings 11 (2021) 969. https://doi.org/10.3390/coatings11080969.

[5]. X. Zou, G. Fang, L. Yuan, X. Tong, X. Zhao, A comparative study of amorphous InGaZnO thin-film transistors with HfO_xN_y and HfO_2 gate dielectrics, Semicond. Sci. Technol. 25 (2010) 055006. https://doi.org/10.1088/0268-1242/25/5/055006.

[6]. J. Song, L. Qian, C. Leung, P. Lai, Improved electrical characteristics of amorphous InGaZnO thin-film transistor with HfLaO gate dielectric by nitrogen incorporation, Appl. Phys. Express 8 (2015) 066503. https://doi.org/10.7567/APEX.8.066503.

[7]. L.X. Qian, P.T. Lai, Fluorinated InGaZnO Thin-Film Transistor With HfLaO Gate Dielectric, IEEE Electron. Device Lett. 35 (2014) 363–365. https://doi.org/10.1109/LED.2013.2296895.

[8]. R. Yao, Z. Zheng, M. Xiong, X. Zhang, X. Li, H. Ning, Z. Fang, W. Xie, X. Lu, J. Peng, Low-temperature fabrication of sputtered high-k HfO_2 gate dielectric for flexible a-IGZO thin film transistors, Appl. Phys. Lett. 112 (2018) 103503. https://doi.org/10.1063/1.5022088.

[9]. P. Ma, J. Sun, G. Zhang, G. Liang, Q. Xin, Y. Li, A. Song, Low–temperature fabrication of HfAlO alloy dielectric using atomic–layer deposition and its application in a low–power device, J. Alloy. Comp. 792 (2019) 543–549. https://doi.org/10.1016/j.jallcom.2019.04.015.

[10]. D. Kim, Y.R. Jeon, B. Ku, C. Chung, T.H. Kim, S. Yang, U. Won, T. Jeong, T. Jeong, C. Choi, Analog Synaptic Transistor with Al-Doped HfO_2 Ferroelectric Thin Film, ACS Appl. Mater. Interfaces 13 (2021) 52743–52753. https://doi.org/10.1021/acsami.1c12735.

[11]. R.N. Bukke, C. Avis, M.N. Naik, J. Jang, Remarkable increase in field effect mobility of amorphous IZTO thin-film transistors with purified ZrO_x gate insulator, IEEE Electron. Device Lett. 39 (2018) 371–374. https://doi.org/10.1109/LED.2018.2791633.

[12]. Z. Chen, L. Lan, J. Peng, Approaching subthreshold-swing limit for thin-film transistors by using a giant-dielectric-constant gate dielectric, RSC Adv. 9 (2019) 27117–27124. https://doi.org/10.1039/C9RA03574E.

[13]. Y. Huang, B. Hekmatshoar, S. Wagner, J.C. Sturm, Top-Gate Amorphous Silicon TFT With Self-Aligned Silicide Source/Drain and High Mobility, IEEE Electron. Device. Lett. 29 (2008) 737–739. https://doi.org/10.1109/LED.2008.2000645.

[14]. G.W. Shim, W. Hong, J.H. Cha, J.H. Park, K.J. Lee, S.Y. Choi, TFT Channel Materials for Display Applications: From Amorphous Silicon to Transition Metal Dichalcogenides, Adv. Mater. 32 (2020) 1907166. https://doi.org/10.1002/adma.201907166.

[15]. F.T. Chien, K.P. Hsueh, Z.J. Hong, K.T. Lin, Y.T. Tsai, H.C. Chiu, A Low Impact Ionization Rate Poly-Si TFT with a Current and Electric Field Split Design, Coatings 9 (2019) 514. https://doi.org/10.3390/coatings9080514.

[16]. W.H. Wang, X.H. Pan, W. Dai, Y.Y. Zeng, Z.Z. Ye, Ultrahigh sensitivity in the amorphous ZnSnO UV photodetector, RSC Adv. 6 (2016) 32715-32720. https://doi.org/10.1039/C6RA02924H.

[17]. A.T. Oluwabi, A. Katerski, E. Carlos, R. Branquinho, A. Mere, M. Krunks, E. Fortunato, L. Pereira, I. O. Acik, Application of ultrasonic sprayed zirconium oxide dielectric in zinc tin oxide-based thin film transistor, J. Mater. Chem. C 8 (2020) 3730–3739. https://doi.org/10.1039/C9TC05127A.

[18]. B. D. Ahn, D.Choi, C. Choi, J.S. Park, The effect of the annealing temperature on the transition from conductor to semiconductor behavior in zinc tin oxide deposited atomic layer deposition, Appl. Phys. Lett. 105 (2014) 092103. https://doi.org/10.1063/1.4895102.

[19]. J.Q. Zhang, J.G. Lu, Y.D. Lu, S.L. Yue, R.K. Lu, X.F. Li, J.H. Zhang, Z.Z. Ye, Dependence of device behaviors on oxygen vacancies in ZnSnO thin-film transistors, Appl. Phys. A. 125 (2019), 362. https://doi.org/10.1007/s00339-019-2646-1.

[20]. C. R. Allemang, T. H. Cho, O. Trejo, S. Ravan, R. E. Rodríguez, N. P. Dasgupta, R. L. Peterso, High-Performance Zinc Tin Oxide TFTs with Active Layers Deposited by Atomic Layer Deposition, Adv. Electron. Mater. 2020, 2000195. https://doi.org/10.1002/aelm.202000195.

[21]. B. Yang, G. He, W. Wang, Y. Zhang, C. Zhang, Y. Xia, X. Xu, Diffusion-activated high performance ZnSnO/Yb_2O_3 thin film transistors and application in low-voltage-operated logic circuits, J. Mater. Sci. Technol. 70 (2021) 49–58. https://doi.org/10.1016/j.jmst.2020.08.042.

[22]. S. Dai, T. Wang, R. Li, Q. Wang, Y. Ma, L. Tian, J. Su, Y. Wang, D. Zhou, X. Zhang, Y. Wang, Preparation and electrical properties of N-doped ZnSnO thinfilm transistors, J. Alloys. Compd. 745 (2018) 256-261. https://doi.org/10.1016/j.jallcom.2018.02.198.

[23]. Y.J. Han, S. H. Lee, S.Y. Bak, T.H. Han, S. Kim, M. Yi, Performance Improvement of ZnSnO Thin-Film Transistors with Low-Temperature Self-Combustion Reaction, Electronics 10 (2021) 1099. https://doi.org/10.3390/electronics10091099.

[24]. D.J. Frank, R.H. Dennard, E. Nowak, P.M. Solomon, Y. Taur and H.S. Philip Wong, Device scaling limits of Si MOSFETs and their application dependencies, Proc. IEEE. 89 (2001) 259–288. https://doi.org/10.1109/5.915374.

[25]. S.S. Gong, M. E. Burnham, N.D. Theodre and D.K. Schroder, Evaluation of QBD for electrons tunneling from the Si/SiO_2 interface compared to electron tunneling from the poly-Si/SiO_2 interface, IEEE Trans. Electron Devices 40 (1993) 1251–1257. https://doi.org/10.1109/16.216429.

[26]. A. Sarkar, L. Velasco, D. Wang, Q. Wang, G. Talasila, L. De Biasi, C. Kübel, T. Brezesinski, S.S. Bhattacharya, H. Hahn, High entropy oxides for reversible energy storage, Nat. Commun. 9 (2018) 3400. https://doi.org/10.1038/s41467-018-05774-5.

[27]. B. Xiao, G. Wu, T. Wang, Z. Wei, Y. Sui, B. Shen, J. Qi, F. Wei, J. Zheng, High-entropy oxides as advanced anode materials for long-life lithium-ion Batteries, Nano Energy 95 (2022) 106962. https://doi.org/10.1016/j.nanoen.2022.106962.

[28]. D. Wang, Z. Liu, S. Du, Y. Zhang, H. Li, Z. Xiao, W. Chen, R. Chen, Y. Wang, Y. Zou, Low-temperature synthesis of small-sized high-entropy oxides for water oxidation, J. Mater. Chem. A 7 (2019) 24211−24216. https://doi.org/10.1039/C9TA08740K.

[29]. T. Li, Y. Yao, B.H. Ko, Z. Huang, Q. Dong, J. Gao, W. Chen, J. Li, S. Li, X. Wang, Carbon-Supported High-Entropy Oxide Nanoparticles as Stable Electrocatalysts for Oxygen Reduction Reactions, Adv. Funct. Mater. 31 (2021) 2010561. https://doi.org/10.1002/adfm.202010561.

[30]. A.Q. Mao, H.Z. Xiang, Z.G. Zhang, K. Kuramoto, H. Zhang, Y.G. Jia, A new class of spinel high-entropy oxides with controllable magnetic properties, J. Magn. Magn Mater. 497 (2020) 165884−165888. https://doi.org/10.1016/j.jmmm.2019.165884.

[31]. Z.W. Huang, K.S. Chang, Spin-coating for fabrication of high-entropy high-k (AlTiVZrHf)O_x films on Si for advanced gate stacks, Ceram. Int. 47 (2021) 22558−22566. https://doi.org/10.1016/j.ceramint.2021.04.267.

[32]. Z. Lou, X. Xu, P. Zhang, L. Gong, Q. Chen, J. Xu, A. Rydosz, F. Gao, Microstructure and dielectric properties of high-entropy $Sr_{0.9}La_{0.1}MeO_3$ (Me: Zr, Sn, Ti, Hf, Mn, Nb) perovskite ceramics, J. Mater. Res. Tech. 21 (2022) 850–855. https://doi.org/10.1016/j.jmrt.2022.09.081.

[33]. V.D. Nguyen, T. Nagata, K.S. Chang, High-throughput methodology for the realization of high-entropy sub-nm equivalent-oxide-thickness high-dielectric-constant Ba(Ti,Zr,Ta,Hf,Mo)O_3 film-based metal-oxide-semiconductor-related device, Mater. Today Phys. 37(2023) 101202. https://doi.org/10.1016/j.mtphys.2023.101202.

[34]. W. Yang, S. Ullah, G. Zheng, The ultra-high electric breakdown strength and superior energy storage properties of $(Bi_{0.2}Na_{0.2}K_{0.2}La_{0.2}Sr_{0.2})TiO_3$ high-entropy ferroelectric thin flms, J. Mater. Sci. Mater. Electron. 35 (2024) 82. https://doi.org/10.1007/s10854-023-11774-z

[35]. A. Salian, P. Pujar, R.V. Vardhan, H. Cho, S. Kim, S. Mandal, Evolution of High Dielectric Permittivity in Low-Temperature Solution Combustion-Processed Phase-Pure High Entropy Oxide (CoMnNiFeCr)O for Thin Film Transistors, ACS Appl. Electron. Matter. (2023). https://doi.org/10.1021/acsaelm.3c00094.

[36]. Z. Liang, W. Wu, X. Fu, H. Ning, G. Su, H. Wang, T. Qiu, Z. Yang, R. Yao, J. Peng, Solution-processed high entropy metal oxides as dielectric layers with high transmittance and performance and application in thin film transistors, Surf. Interf. 40 (2013) 103147. https://doi.org/10.1016/j.surfin.2023.103147.

[37]. K.S. Chang, H.C. Feng, C.L. Chen, W.C. Lu, Substantial Enhancement of Dielectric Properties of Amorphous Y_2O_3-TiO_2 Composition Spreads Through N_2 Doping by Using Combinatorial Sputtering, IEEE Trans. on Electron Devices 61 (2014) 2125. https://doi.org/10.1109/TED.2014.2318303

[38]. Y. Liang, B. Luo, H. Dong, D. Wang, Electronic structure and transport properties of sol-gel-derived high-entropy Ba(Zr0.2Sn0.2Ti0.2Hf0.2Nb0.2)O3 thin films, Ceram. Int. 47 (2021) 20196−20200. https://doi.org/10.1016/j.ceramint.2021.04.026.

[39]. X. L. Li, H. B. Lu, M Li, Z. Mai, Characteristics of the low electron density surface layer on $BaTiO_3$ thin films, Appl. Phys. Lett. 92 (2008) 012902. https://doi.org/10.1063/1.2828339.

[40]. K.S. Hong, M.G. Ha, J.S. Bae, J.S. Kim, Y.R. Bae, C.W. Ahn, I.W. Kim, J.P. Kim,

Structural characteristics and chemical bonding states with temperature in barium titanate nanopowders prepared by using the solvothermal method, Current. Appl. Phys. 15 (2015) 1377–1383. https://doi.org/10.1016/j.cap.2015.06.028.

[41]. Y. Noh, Y. Kim, H. Han, S. Park, W. Yoon, S. Lee, J.G. Kim, Y. Kim, H. Ju Kim, W.B. Kim, Heat Treatment–Controlled Morphology Modification of Electrospun Titanium Oxynitride Nanowires for Capacitive Energy Storage and Electrocatalytic Reactions, Energy Technol. 8 (2020) 2000184. https://doi.org/10.1002/ente.202000184.

[42]. J. Huang, A. Meng, Z. Zhang, S. Xiao, X. Guo, X. Wu, S. Huang, G. Ma, P. Han, B. He, Enhanced Visible-Light-Driven Photoelectrochemical Activity in Nitrogen-Doped TiO2/Boron-Doped Diamond Heterojunction Electrodes. ACS Appl. Energy Mater. 5 (2022) 7144−7156. https://doi.org/10.1021/acsaem.2c00679.

[43]. J.C. Chang, F. Eriksson, M.A. Sortica, G. Greczynski, B. Bakhit, Z. Hu, D. Primetzhofer, L. Hultman, J. Birch, C.L. Hsiao, Orthorhombic $Ta_{3-x}N_{5-y}O_y$ thin films grown by unbalanced magnetron sputtering: The role of oxygen on structure, composition, and optical properties, Surf. Coat. Tech. 406 (2021) 126665. https://doi.org/10.1016/j.surfcoat.2020.126665.

[44]. R.V. Gonçalves, R. Wojcieszak, P.M. Uberman, S.R. Teixeira, L.M. Rossi, Insights into the active surface species formed on Ta_2O_5 nanotubes in the catalytic oxidation of CO, Phys. Chem. Chem. Phys. 16 (2014) 5755−5762. https://doi.org/10.1039/C3CP54887B.

[45]. G. He, J. Liu, H. Chen, Y. Liu, Z. Sun, X Chen, M. Liud, L. Zhang, Interface control and modification of band alignment and electrical properties of HfTiO/GaAs gate stacks by nitrogen incorporation, J. Mater. Chem. C 2 (2014) 5299–5308. https://doi.org/10.1039/c4tc00572d.

[46]. X. Luo, Y. Li, H. Yang, Y. Liang, K. He, W. Sun, H.H. Lin, S. Yao, X. Lu, L. Wan, Z. Feng, Investigation of HfO2 Thin Films on Si by X-ray Photoelectron Spectroscopy, Rutherford Backscattering, Grazing Incidence X-ray Diffraction and Variable Angle Spectroscopic Ellipsometry, Crystals 8 (2018) 248. https://doi.org/10.3390/cryst8060248.

[47]. Z. Azdad, L. Marot, L. Moser, R. Steiner, E. Meyer, Valence band behaviour of zirconium oxide, Photoelectron and Auger spectroscopy study, Sci. Rep. 8 (2018) 16251. https://doi.org/10.1038/s41598-018-34570-w.

[48]. G.I. Cubillos, E. Romero, A.U. Perez, ZrN-ZrO_xN_y vs ZrO_2-ZrO_xN_y coatings deposited via unbalanced DC magnetron sputtering, Sci. Rep. 11 (2021) 18926. https://doi.org/10.1038/s41598-021-98052-2.

[49]. B. Jin, P. Chen, H. Chu, D. Zhang, S.S Cui, X. Zhou, M. Yang, Tunable built-in electric fields enable high-performance one-dimensional co-axial MoOx/ MoON heterojunction nanotube arrays for thin-film pseudocapacitive charge storage devices, J. Mater. Chem. A 9 (2021) 13263–13270. https://doi.org/10.1039/d1ta02360h.

[50]. N. Selvakumar, N.T. Manikandanath, A. Biswas, H.C. Barshilia, Design and fabrication of highly thermally stable HfMoN/HfON/Al_2O_3 mtandem absorber for solar thermal power generation applications, Sol. Energy Mater. Sol. Cells 102 (2012) 86–92. http://dx.doi.org/10.1016/j.solmat.2012.03.021.

[51]. C.X. Huang, J. Li, D.Y. Zhong, C.Y. Zhao, W.Q. Zhu, J.H. Zhang, X.Y. Jiang, Z.L. Zhang, Atomic layer deposition deposited high dielectric constant (κ) ZrAlOx gate insulator enabling high performance ZnSnO thin film transistors, Supperlattices Microstruct. 109 (2017) 852–859. https://doi.org/10.1016/j.spmi.2017.06.011.

[52]. S. Jiang, X. Yang, J. Zhang, X. Li, Solution-processed stacked TiO_2 and Al_2O_3 dielectric layers for high mobility thin film transistor, AIP Adv. 8 (2018) 085109. https://doi.org/10.1063/1.5034497.

[53]. B. Yang, G. He, L. Zhu, C. Zhang, Y. Zhang, Y. Xia, F. Alam, Z. Sun, Low-Voltage-Operating Transistors and Logic Circuits Based on a Water-Driven ZrGdOx Dielectric with Low-Cost ZnSnO, ACS Appl. Electron. Mater. 1 (2019) 625−636. https://doi.org/10.1021/acsaelm.9b00110.

[54]. Q. Zhang, G. Xia, L. Li, W. Xia, H. Gong, S. Wang, High-performance Zinc-Tin-Oxide thin film transistors based on environment friendly solution process, Curr. Appl. Phys. 19 (2019) 174–181. https://doi.org/10.1016/j.cap.2018.10.012.

[55]. B. Yang, Y. Liu, S. Lan, L.Dou, C.W. Nan, Y.H. Lin, High-entropy design for dielectric materials: Status, challenges, and beyond, J. Appl. Phys. 133 (2023) 110904. https://doi: 10.1063/5.0138877

[56]. N.N. Mude, R.N. Bukke, J.K. Saha, C. Avis, J. Jang, Highly Stable, Solution Processed Ga Doped IZTO Thin Film Transistor by Ar/O_2 Plasma Treatment, Adv. Electron. Mater. 6 (2019) 1900768. https://doi.org/10.3390/nano10050976.

[57]. X. Yang, S. Jiang, J. Li, J.H. Zhang, X.F. Li, Improvement of the long-term stability of ZnSnO thin film transistors by tungsten incorporation using a solution-process method, RSC Adv.8 (2018) 20990–20995. https://doi.org/10.1039/C8RA02925C.

[58]. L. C. Liu, J.F. Chen, J.S. Jeng, Role of oxygen vacancies on the bias illumination stress stability of solution-processed zinc tin oxide thin film transistors, Appl. Phys. Lett. 105 (2014) 023509. https://doi.org/10.1063/1.4890579.

[59]. J. Kim, S. Bang, S. Lee, S. Shin, J. Park, H. Seo, H. Jeon, A study on H_2 plasma treatment effect on a-IGZO thin film transistor, J. Mater. Res. 27 (2012) 2318–2325. https://doi.org/10.1557/jmr.2012.199.

[60]. T.H. Chang, C.J. Chiu, W.Y. Weng, S.J. Chang, T.Y. Tsai, Z.D. Huang, High responsivity of amorphous indium gallium zinc oxide phototransistor with Ta_2O_5 gate dielectric. Appl. Phys. Lett. 101 (2012) 261112. https://doi.org/10.1063/1.4773307.

[61]. X. Liu, X. Liu, J. Wang, C. Liao, X. Xiao, S. Guo, C. Jiang, Z. Fan, T. Wang, X. Chen, W. Lu, W. Hu, L. Liao, Transparent, high-performance thin-film transistors with an InGaZnO/alignedSnO2-nanowire composite and their application in photodetectors. Adv. Mater. 26 (2014) 7399−7404. https://doi.org/10.1002/adma.201401732

[62]. J. Yu, K. Javaid, L. Liang, W. Wu, Y. Liang, A. Song, H. Zhang, W. Shi, T.C. Chang, H. Cao, High-Performance Visible-Blind Ultraviolet Photodetector Based on IGZO TFT Coupled with p−n Heterojunction, ACS Appl. Mater. Interfaces 10 (2018) 8102−8109. https:// doi.org/10.1021/acsami.7b16498

[63]. P.H. Chen, Y.C. Tsao, Y.C. Chien, H.C. Chiang, H.M. Chen, Y.H. Lu, C.C. Shih, M.C. Tai, G.F. Chen, Y.L. Tsai, H.C. Huang, T.M. Tsai, T.C. Chang, A Dual-Gate InGaZnO4-Based Thin-Film Transistor for High-Sensitivity UV Detection, Adv.Matter. Tech. 4(2019) 1900106. https:// doi.org/10.1002/admt.20190010.

Table caption

Table 1. Electrical performance of our TFT device and various other high-*k*-materials-based TFTs reported in the literature.

Table 2. Performance of our UV photodetectors and various TFT-based photodetectors reported in the literature.

Figure caption

Figure 1. Hybrid-DFT-based calculation of the energy band structures of (a) N-doped Ba(Ti,Zr,Mo,Hf,Ta)O_3 and (b) ZnSnO. (c) Aligned energy band structures and the resulting $E_{C,\ offset}$ values.

Figure 2. (a) XRD 3D patterns obtained from 100 locations across the N-doped Ba(Ti,Zr,Mo,Hf,Ta)O_3 film library (top-left inset). The top-view image of the 3D patterns is displayed in the top-right inset. (b) Ternary diagram of elemental variations (at.%) across the film library. (c) ΔS_{conf} of the compositions at these 100 locations [top-left inset in (a)].

Figure 3. High-resolution XPS spectra of $Ba(Ti_{0.17}Zr_{0.30}Mo_{0.26}Hf_{0.13}Ta_{0.13})(O_{2.60}N_{0.40})$: (a) Ba 3d, (b) Ti 2p, (c) Ta 4f, (d) Hf 4f, (e) Zr 3d, (f) Mo 3d, (g) O 1s, and (h) N 1s.

Figure 4. TEM-EDS analysis of one TFT device composed of N-doped Ba(Ti,Zr,Mo,Hf,Ta)O_3 in the high-entropy region (red circle in Figure 2c): (a) scanning area, (b) elements of (i) Al, (ii) Zn, (iii) Sn, (iv) In, (v) Ba, (vi) Ti, (vii) Zr, (viii) Hf, (ix) Ta, (x) Mo, and (xi) O, and (c) associated spectrum.

Figure 5. 3D ternary diagrams of the dielectric property of 100 MIM configurations against the elemental composition: (a) C_{ox} measured at 1 kHz and (b) J_L measured at 1 V.

Figure 6. (a) Four TFT devices at different locations (i–iv) along the direction of composition variation in the film library. (b) (i)–(iv) Associated HRTEM cross-sectional images.

Figure 7. 3D ternary diagrams of the dielectric property of 100 MIM configurations against their elemental compositions: (a) *k* at 1 kHz, (b) EOT, and (c) tan δ at 1 kHz.

Figure 8. Electrical performance of one of the favorable TFTs. (a) Output characteristic. The upper right inset shows 63 patterned TFTs on the entire library, and the red mark indicates the TFT chosen for measurement. The lower left inset displays voltage supplies among the three terminals. (b) Transfer characteristic. The lower right inset is a photograph of the resulting TFT applied to a circuit board as a switch. (c) Long-term stability of the TFT.

Figure 9. PGBSI study of the TFT at V_{DS} = 2 V and PGBS = 3 V for various times. (a) Transfer curves without UV illumination. The lower right and upper left insets show the measurement procedure and detailed variations in $I_{DS,\ max}$ and V_T, respectively. (b) Energy band diagram without UV illumination. (c) Transfer curves with UV illumination. The inset shows detailed variations in $I_{DS,\ max}$ and V_T. (d) Energy band diagram with UV illumination.

Figure 10. Transfer characteristics and $I_{DS,\ max}$ (blue) and ΔV_T (orange) values (insets) of the TFT at V_{DS} = 2 V, PGBS = 3 V, various stress times (0–3600 s), and four different temperatures: (a) 50 °C. (b) 100 °C. (c) 150 °C, and (d) 180 °C.

Figure 11. Plots of ln(I_{DS}) against 1/KT of the TFT at various V_{GS}, and $E_A(V_{GS})$ against V_{GS} (insets) of the TFT. (a) Without PGBS or UV illumination, (b) without PGBS and with UV illumination, (c) with PGBS and without UV illumination, and (d) with both PGBS and UV illumination.

Figure 12. UV-sensing capability of the TFT. (a) Transfer characteristics measured at V_{DS} = 8 V under dark conditions and illumination at various wavelengths. Inset: the measurement setup. (b) Output curves measured at V_{GS} = –6 V. The upper right and lower right insets depict energy band diagrams associated with visible light and UV illumination, respectively. (c) Photocurrent durability measured at V_{GS} = –6 V and V_{DS} = 8 V under various UV illuminations. (d) Single-cycle evolution of the photocurrent response under 253-nm illumination.

Figure 13. Flexibility study of the TFT fabricated on PI substrate. (a) Transfer curve without deformation. (b) Transfer curves measured at various bending levels (R = 5, 8, and 12 mm). Inset: a photograph of the device bent at R = 8 mm. (c) Photocurrent durability measured at V_{GS} = – 6 V and V_{DS} = 8 V under UV illumination (253 nm). (d) Electrical performance at various bending levels.

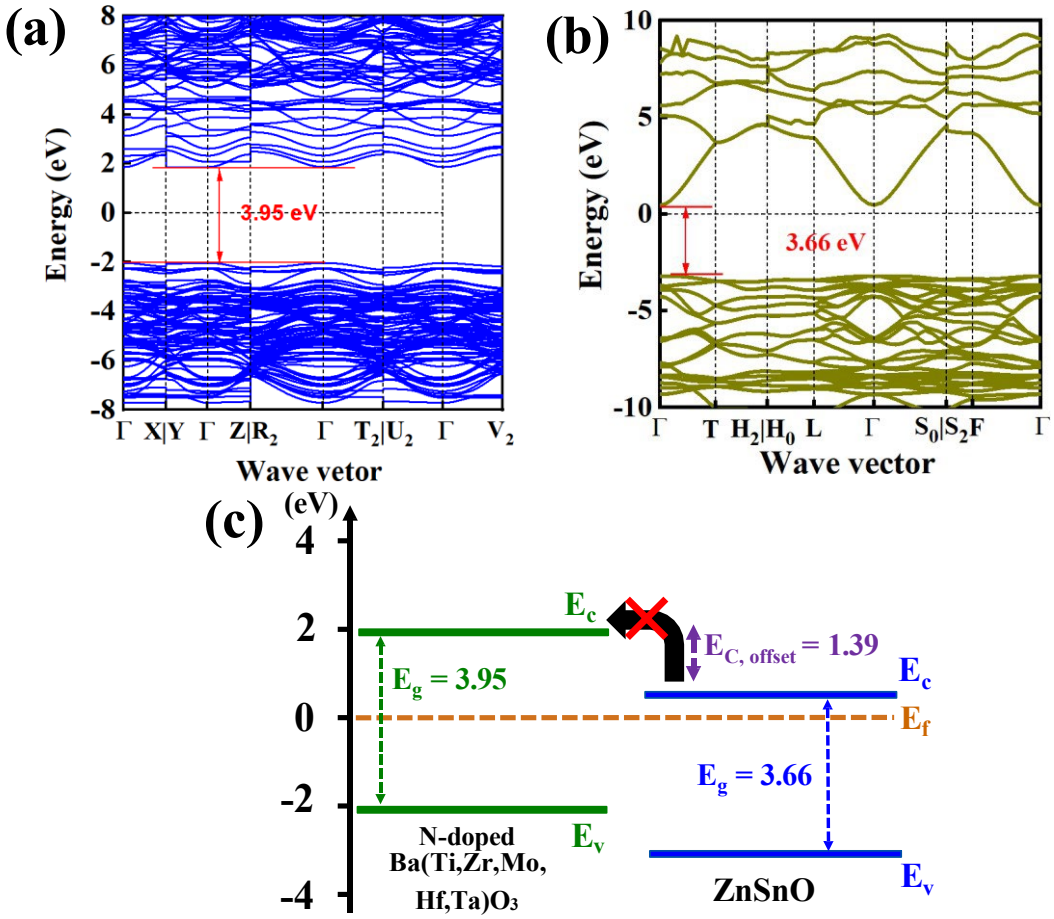
Table 1.

Dielectric	I_{ON}/I_{OFF} ratio	D_{it} ($eV^{-1}cm^{-2}$)	Mobility ($cm^2 \cdot V^{-1} \cdot s^{-1}$)	V_T (V)	SS ($V \cdot dec^{-1}$)	Ref.
N-doped $Ba(Hf,Zr,Mo,Ta,Ti)O_3$	7×10^8	9.59×10^{10}	93.84	0.02	0.062	This work
ZrO_x	10^6	5.7×10^{12}	4.61	0.03	0.25	[17]
SiO_2	8×10^8	1.5×10^{12}	23.6	-1.5	0.65	[19]
$ZrAlO_x$	8×10^7	5.13×10^{11}	12.5	0.3	0.15	[50]
$TiO_2/Al_2O_3/TiO_2/Al_2O_3/TiO_2$ (TATAT)	1.2×10^8	1.1×10^{11}	86.6	0.56	0.2	[51]
TiAlO	1.7×10^7	N/A	6.83	1.57	0.26	[51]
$ZrGdO_x$	1.1×10^6	N/A	2.9	0.7	0.092	[52]
$ZrTiO_x$	10^5 - 10^6	N/A	17.9	0.96	N/A	[53]

Table 2.

Materials	Structure	Sensitivity	Responsivity (A/W)	τ_g (s)	τ_d (s)	Ref.
IGZO/Ta_2O_5	TFT	10^6	6.4	N/A	N/A	[60]
IGZO/SnO_2	TFT	10^4	328.6	N/A	N/A	[61]
PEDOT:PSS/SnO_x/IGZO	TFT & pn	10^5	984	N/A	N/A	[62]
ZnSnO	TFT	103 654	808	2.18	2.72	[16]
InGaZnO	TFT	≈10^6	N/A	0.4	0.35	[63]
ZnSnO	TFT	2×10^6	≈1171.85	0.037	0.025	This work

Figure 1.


(a)
Energy (eV)
3.95 eV
Γ X|Y Γ Z|R2 Γ T2|U2 Γ V2
Wave vetor
(b)
Energy (eV)
3.66 eV
Γ T H2|H0 L Γ S0|S2F Γ
Wave vector
(c)
(eV)
Ec
EC, offset = 1.39
Eg = 3.95
Ec
Ef
Eg = 3.66
N-doped
Ba(Ti,Zr,Mo,
Hf,Ta)O3
Ev
ZnSnO
Ev

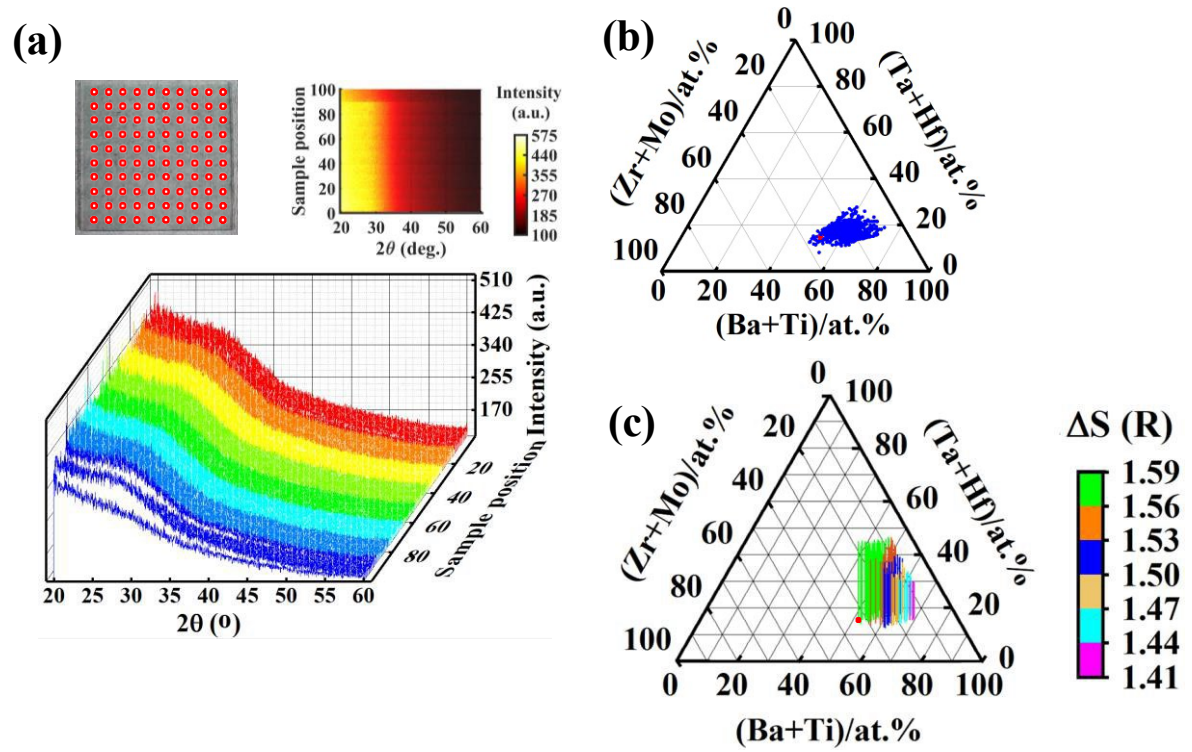

(a)
Sample position
Intensity (a.u.)
2θ (deg.)
Intensity (a.u.)
Sample position
2θ (°)
(b)
(Zr+Mo)/at.%
(Ta+Hf)/at.%
(Ba+Ti)/at.%
(c)
(Zr+Mo)/at.%
(Ta+Hf)/at.%
(Ba+Ti)/at.%
ΔS (R)
1.59
1.56
1.53
1.50
1.47
1.44
1.41

Figure 3.

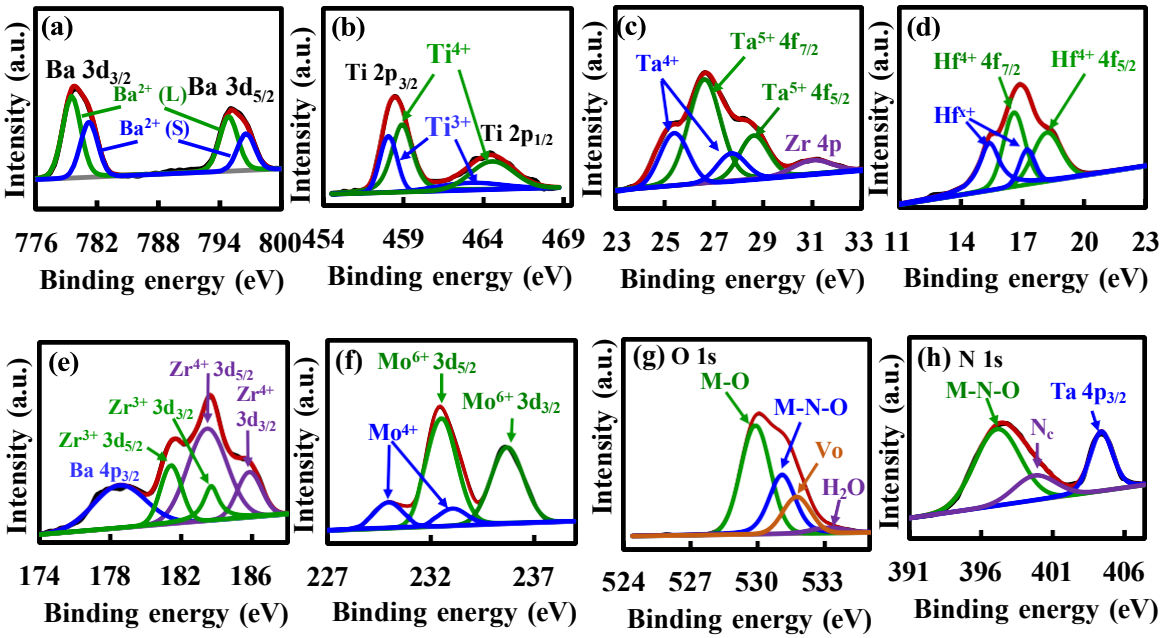

(a)
Ba 3d3/2
Ba2+ (L)
Ba 3d5/2
Ba2+ (S)
Intensity (a.u.)
776 782 788 794 800
Binding energy (eV)
(b)
Ti 2p3/2
Ti4+
Ti3+
Ti 2p1/2
454 459 464 469
Binding energy (eV)
(c)
Ta4+
Ta5+ 4f7/2
Ta5+ 4f5/2
Zr 4p
23 25 27 29 31 33
Binding energy (eV)
(d)
Hf4+ 4f7/2
Hf4+ 4f5/2
Hfx+
11 14 17 20 23
Binding energy (eV)
(e)
Zr4+ 3d5/2
Zr3+ 3d3/2
Zr4+ 3d3/2
Zr3+ 3d5/2
Ba 4p3/2
174 178 182 186
Binding energy (eV)
(f) Mo6+ 3d5/2
Mo6+ 3d3/2
Mo4+
227 232 237
Binding energy (eV)
(g) O 1s
M-O
M-N-O
Vo
H2O
524 527 530 533
Binding energy (eV)
(h) N 1s
M-N-O
Ta 4p3/2
Nc
391 396 401 406
Binding energy (eV)

Figure 4.

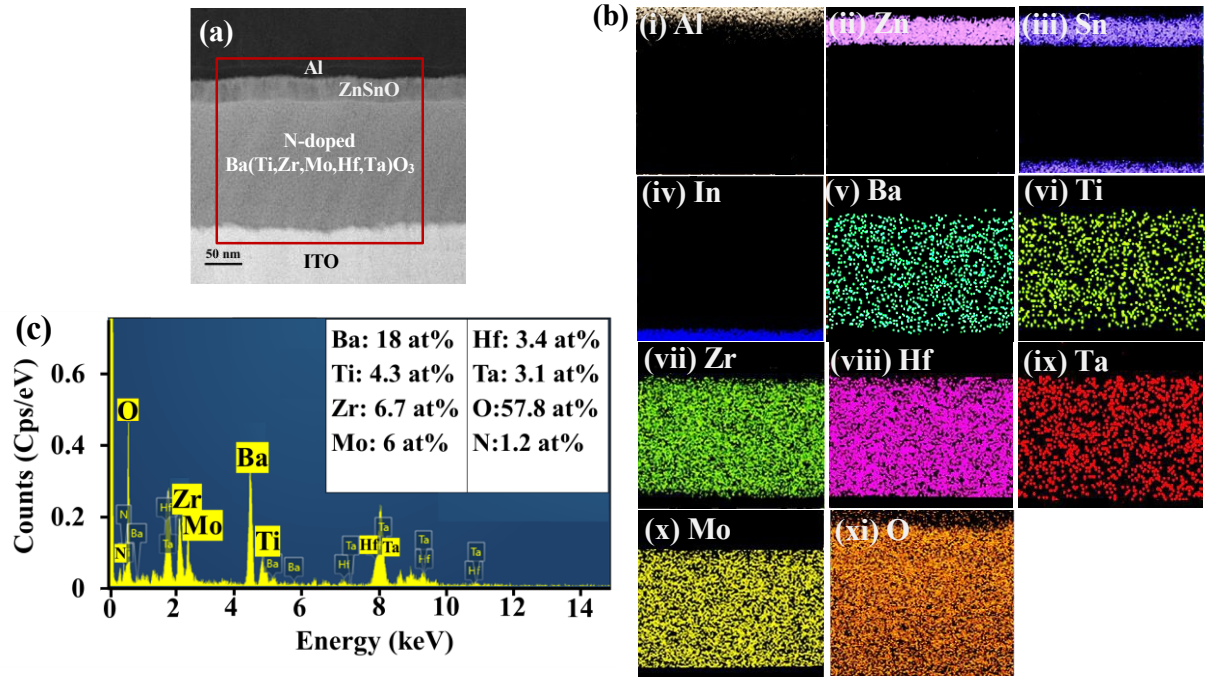

(a)
Al
ZnSnO
N-doped
Ba(Ti,Zr,Mo,Hf,Ta)O3
50 nm
ITO
(b)
(i) Al
(ii) Zn
(iii) Sn
(iv) In
(v) Ba
(vi) Ti
(vii) Zr
(viii) Hf
(ix) Ta
(x) Mo
(xi) O
(c)
Ba: 18 at%
Hf: 3.4 at%
Ti: 4.3 at%
Ta: 3.1 at%
Zr: 6.7 at%
O:57.8 at%
Mo: 6 at%
N:1.2 at%
Counts (Cps/eV)
Energy (keV)

Figure 5.

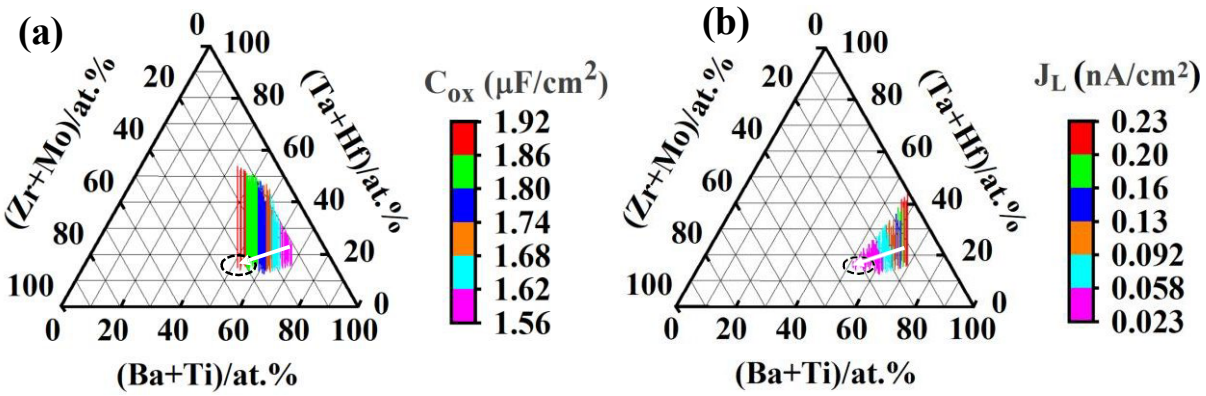

(a)
(Zr+Mo)/at.%
(Ta+Hf)/at.%
(Ba+Ti)/at.%
0
20
40
60
80
100
C_ox (μF/cm²)
1.92
1.86
1.80
1.74
1.68
1.62
1.56
(b)
(Zr+Mo)/at.%
(Ta+Hf)/at.%
(Ba+Ti)/at.%
J_L (nA/cm²)
0.23
0.20
0.16
0.13
0.092
0.058
0.023

Figure 6.

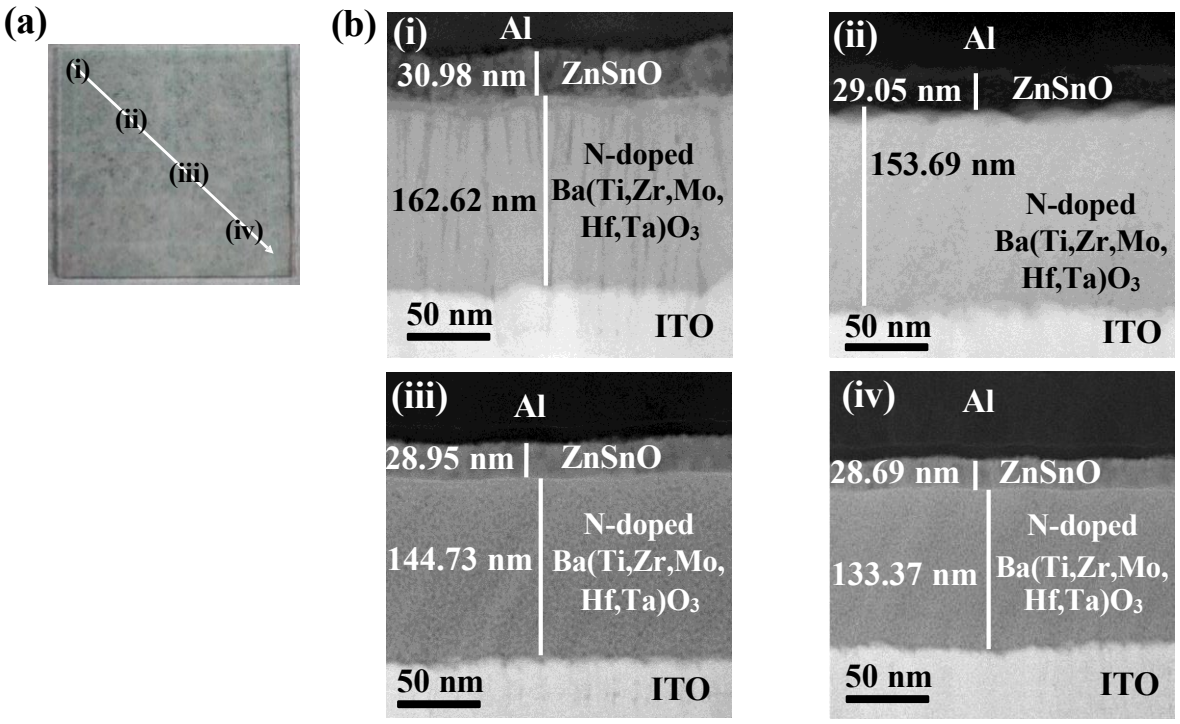

(a)
(i)
(ii)
(iii)
(iv)
(b)
(i)
Al
30.98 nm
ZnSnO
N-doped
Ba(Ti,Zr,Mo,
Hf,Ta)O3
162.62 nm
50 nm
ITO
(ii)
Al
29.05 nm
ZnSnO
153.69 nm
N-doped
Ba(Ti,Zr,Mo,
Hf,Ta)O3
50 nm
ITO
(iii)
Al
28.95 nm
ZnSnO
N-doped
Ba(Ti,Zr,Mo,
Hf,Ta)O3
144.73 nm
50 nm
ITO
(iv)
Al
28.69 nm
ZnSnO
N-doped
Ba(Ti,Zr,Mo,
Hf,Ta)O3
133.37 nm
50 nm
ITO

Figure 7.

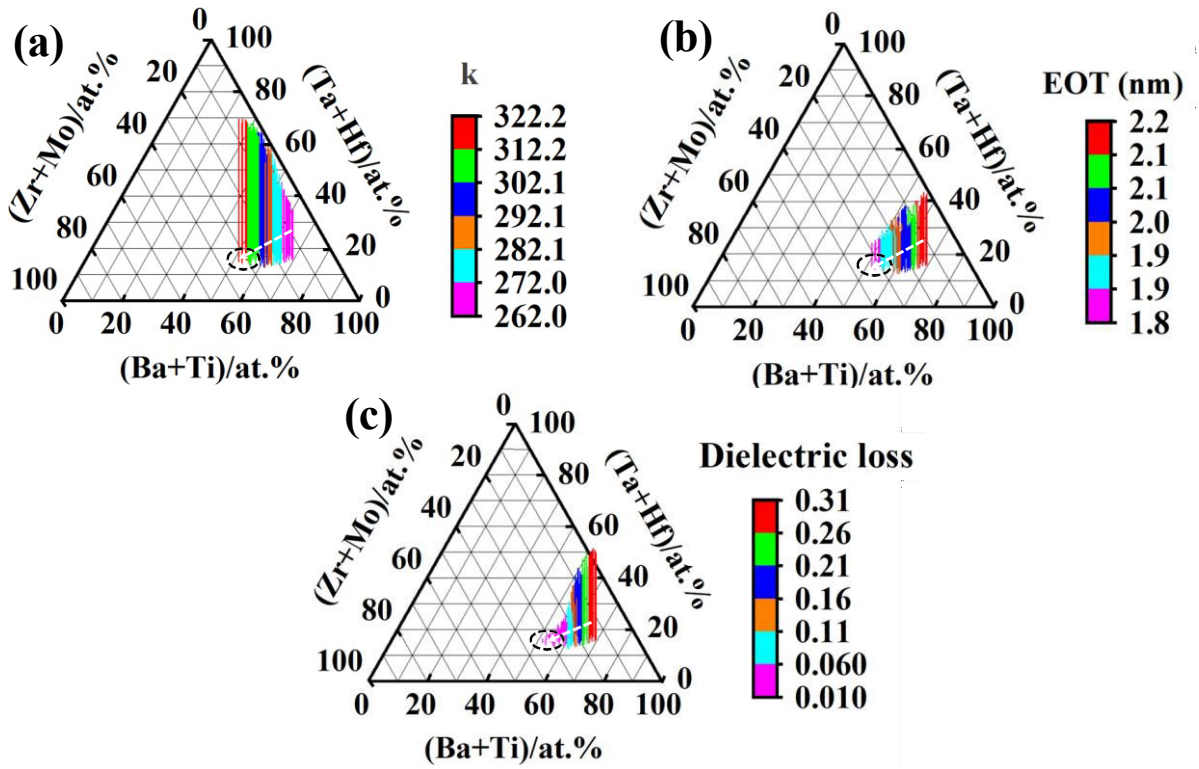

(a)
(Zr+Mo)/at.%
(Ta+Hf)/at.%
(Ba+Ti)/at.%
k
322.2
312.2
302.1
292.1
282.1
272.0
262.0
(b)
(Zr+Mo)/at.%
(Ta+Hf)/at.%
(Ba+Ti)/at.%
EOT (nm)
2.2
2.1
2.1
2.0
1.9
1.9
1.8
(c)
(Zr+Mo)/at.%
(Ta+Hf)/at.%
(Ba+Ti)/at.%
Dielectric loss
0.31
0.26
0.21
0.16
0.11
0.060
0.010

Figure 8.

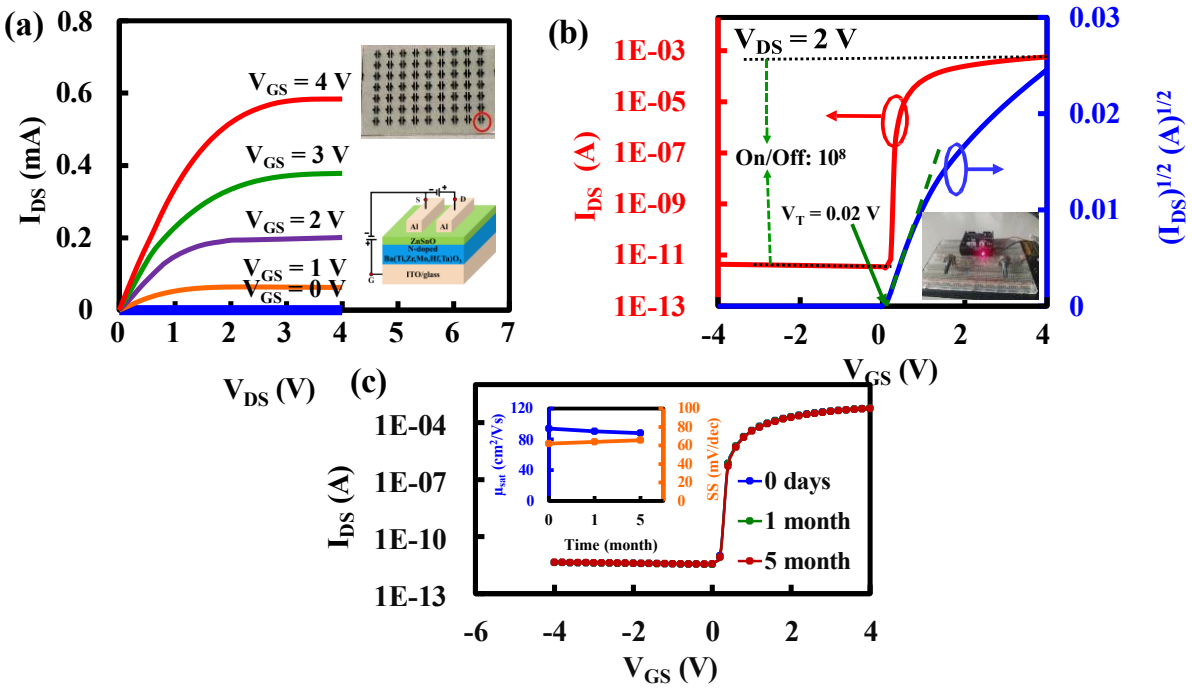

(a)
I_{DS} (mA)
V_{DS} (V)
V_{GS} = 4 V
V_{GS} = 3 V
V_{GS} = 2 V
V_{GS} = 1 V
V_{GS} = 0 V
(b)
V_{DS} = 2 V
On/Off: 10^8
V_T = 0.02 V
I_{DS} (A)
$(I_{DS})^{1/2}$ $(A)^{1/2}$
V_{GS} (V)
(c)
I_{DS} (A)
V_{GS} (V)
μ_{sat} (cm^2/Vs)
SS (mV/dec)
Time (month)
0 days
1 month
5 month

Figure 9.

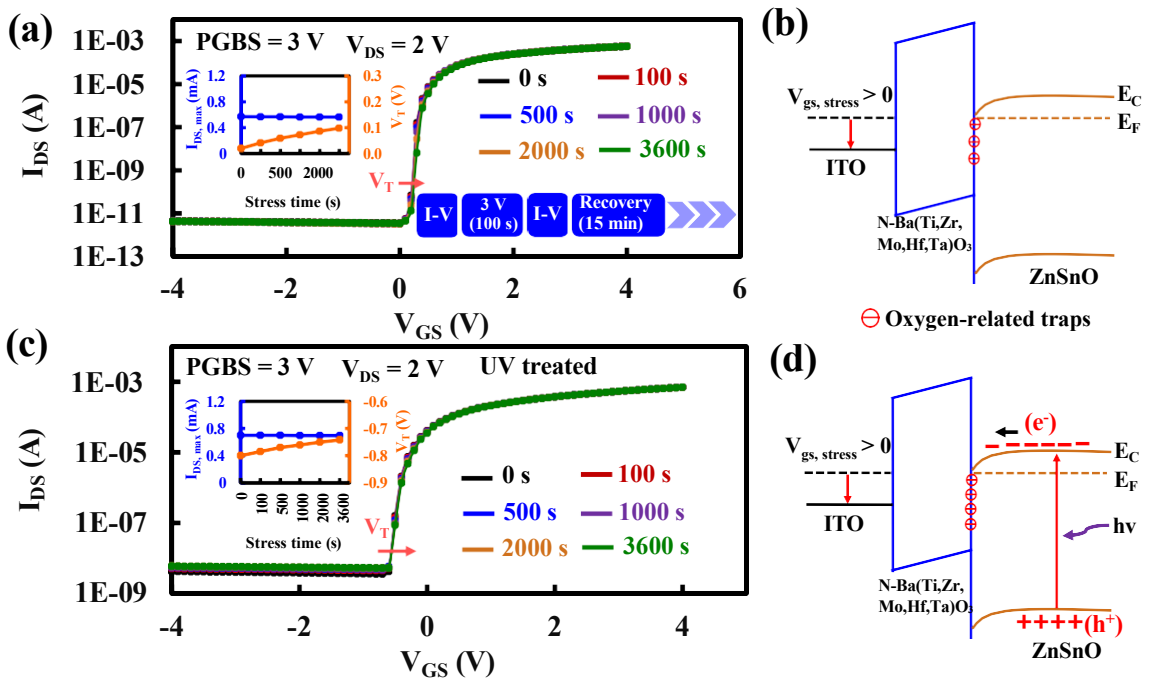

(a)
PGBS = 3 V
V_DS = 2 V
I_DS (A)
V_GS (V)
Stress time (s)
V_T
0 s
100 s
500 s
1000 s
2000 s
3600 s
I-V
3 V (100 s)
I-V
Recovery (15 min)
(b)
V_gs, stress > 0
ITO
N-Ba(Ti,Zr, Mo,Hf,Ta)O3
ZnSnO
E_C
E_F
⊖ Oxygen-related traps
(c)
PGBS = 3 V
V_DS = 2 V
UV treated
(d)
(e-)
hv
++++(h+)

Figure 10.

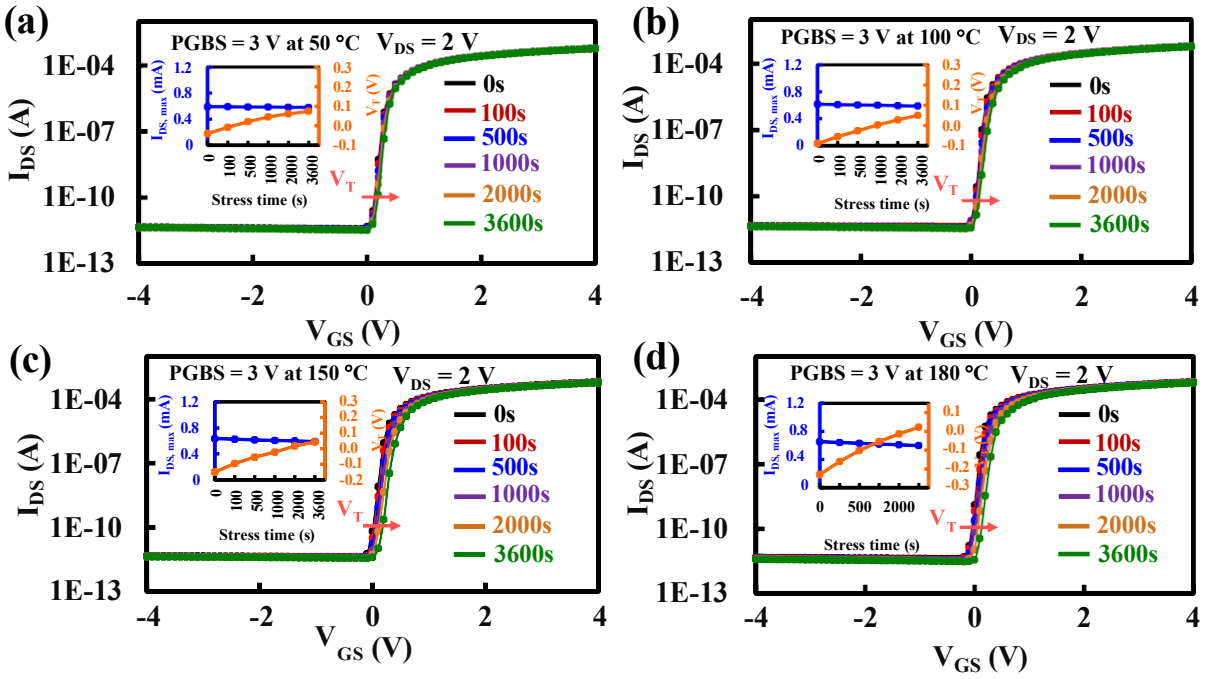

(a)
PGBS = 3 V at 50 °C V_DS = 2 V
(b)
PGBS = 3 V at 100 °C V_DS = 2 V
(c)
PGBS = 3 V at 150 °C V_DS = 2 V
(d)
PGBS = 3 V at 180 °C V_DS = 2 V
I_DS (A)
V_GS (V)
I_DS, max (mA)
V_T (V)
Stress time (s)
V_T
0s
100s
500s
1000s
2000s
3600s

Figure 11.

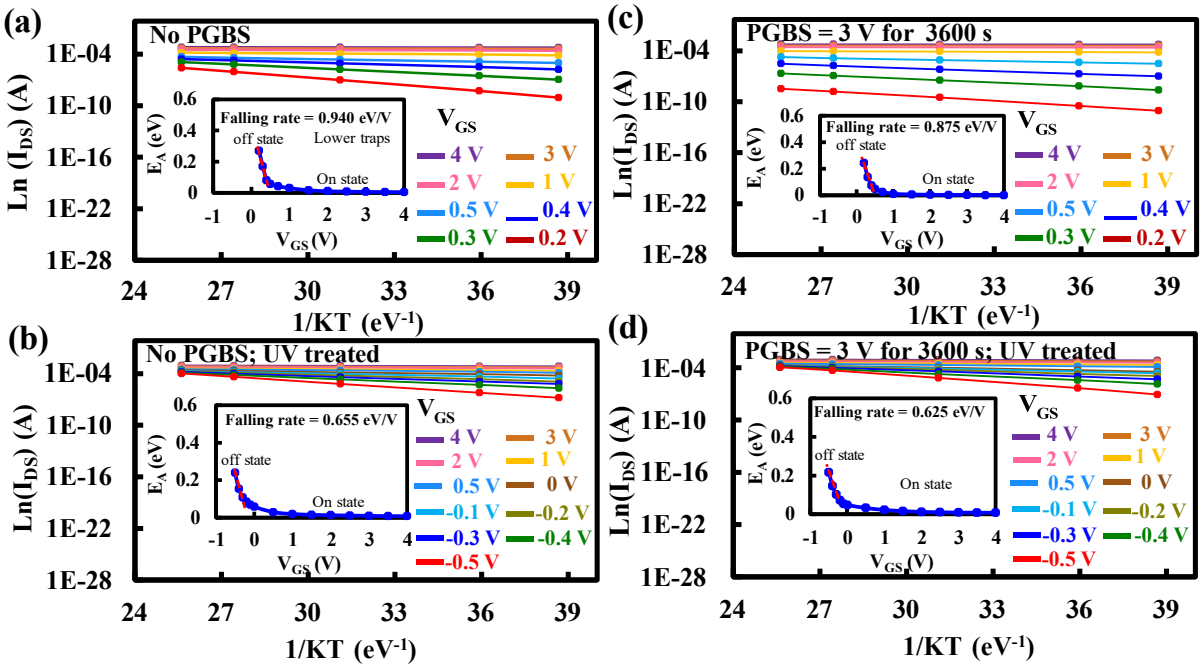

(a)
No PGBS
Falling rate = 0.940 eV/V
off state
Lower traps
On state
E_A (eV)
V_{GS} (V)
V_{GS}
4 V
3 V
2 V
1 V
0.5 V
0.4 V
0.3 V
0.2 V
Ln (I_{DS}) (A)
1E-04
1E-10
1E-16
1E-22
1E-28
24
27
30
33
36
39
1/KT (eV^{-1})
(b)
No PGBS; UV treated
Falling rate = 0.655 eV/V
0 V
-0.1 V
-0.2 V
-0.3 V
-0.4 V
-0.5 V
(c)
PGBS = 3 V for 3600 s
Falling rate = 0.875 eV/V
(d)
PGBS = 3 V for 3600 s; UV treated
Falling rate = 0.625 eV/V

Figure 12.

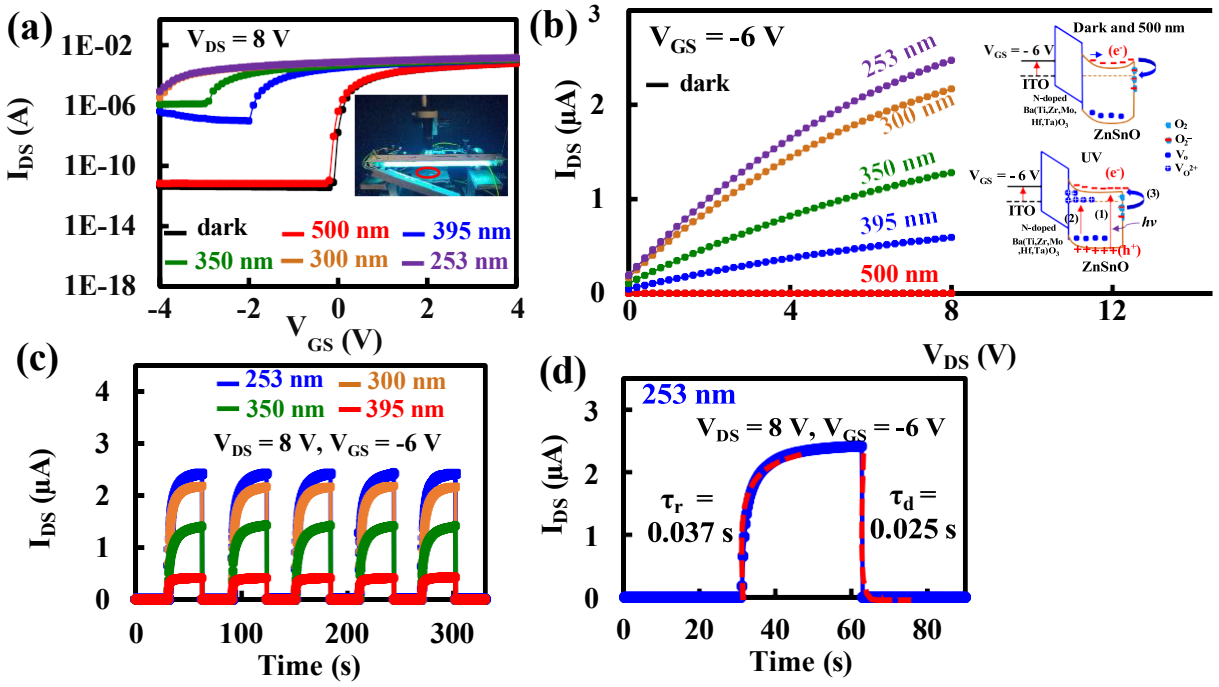
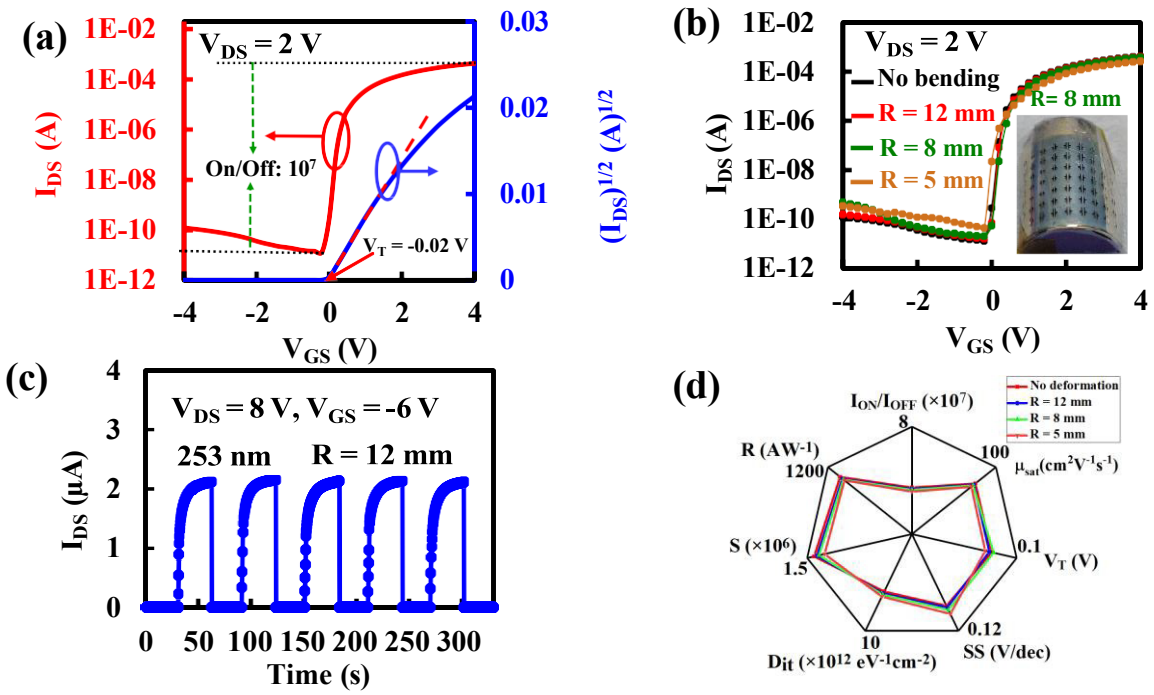

(a)
V_{DS} = 8 V
I_{DS} (A)
1E-02
1E-06
1E-10
1E-14
1E-18
dark
500 nm
395 nm
350 nm
300 nm
253 nm
-4
-2
0
2
4
V_{GS} (V)
(b)
V_{GS} = -6 V
dark
253 nm
300 nm
350 nm
395 nm
500 nm
I_{DS} (μA)
0
1
2
3
0
4
8
12
V_{DS} (V)
Dark and 500 nm
V_{GS} = - 6 V
ITO
N-doped Ba(Ti,Zr,Mo, Hf,Ta)O_3
ZnSnO
(e⁻)
UV
(1)
(2)
(3)
hν
(h⁺)
O_2
O_2^-
V_o
V_O^{2+}
(c)
253 nm
300 nm
350 nm
395 nm
V_{DS} = 8 V, V_{GS} = -6 V
I_{DS} (μA)
0
1
2
3
4
0
100
200
300
Time (s)
(d)
253 nm
V_{DS} = 8 V, V_{GS} = -6 V
τ_r = 0.037 s
τ_d = 0.025 s
I_{DS} (μA)
0
1
2
3
0
20
40
60
80
Time (s)

Figure 13.


(a)
1E-02
1E-04
1E-06
1E-08
1E-10
1E-12
I_{DS} (A)
V_{DS} = 2 V
On/Off: 10^7
V_T = -0.02 V
0.03
0.02
0.01
0
$(I_{DS})^{1/2}$ (A)$^{1/2}$
-4 -2 0 2 4
V_{GS} (V)
(b)
V_{DS} = 2 V
No bending
R = 12 mm
R = 8 mm
R = 5 mm
R= 8 mm
I_{DS} (A)
V_{GS} (V)
(c)
V_{DS} = 8 V, V_{GS} = -6 V
253 nm
R = 12 mm
I_{DS} (μA)
0 1 2 3 4
0 50 100 150 200 250 300
Time (s)
(d)
No deformation
R = 12 mm
R = 8 mm
R = 5 mm
I_{ON}/I_{OFF} ($\times 10^7$)
8
100
μ_{sat}($cm^2V^{-1}s^{-1}$)
0.1
V_T (V)
0.12
SS (V/dec)
10
D_{it} ($\times 10^{12}$ $eV^{-1}cm^{-2}$)
1.5
S ($\times 10^6$)
1200
R (AW^{-1})